

Size, shape, density, and atmospheric limit of (50000) Quaoar revealed from 14 years of stellar occultation

GIULIANO MARGOTI ^{1,2,3} FELIPE BRAGA-RIBAS ^{2,1,3,4} JOSÉ LUIS ORTIZ ⁵ BRUNO SICARDY ⁶
JOSSELIN DESMARS ^{6,7} MORGADO, B. E. ⁸ EROS DE OLIVEIRA GRADOVSKI ^{1,2,3} CHRYSTIAN LUCIANO PEREIRA ^{1,3}
PABLO SANTOS-SANZ ⁵ ALTAIR RAMOS GOMES-JÚNIOR ^{9,3} JULIO IGNACIO BUENO DE CAMARGO ^{1,3}
MARCELO ASSAFIN ^{8,3} VIEIRA-MARTINS ROBERTO ¹ YUCEL KILIC ^{5,4} DAMYA SOUAMI ^{4,10} RENÉ DUFFARD ⁵
GUSTAVO BENEDETTI-ROSSI ³ TIAGO PINHEIRO ¹ MAÍSA POIANI ⁹ EDUARDO RONDÓN ¹ MARCELO EMILIO ^{11,1}
DAVE HERALD ¹² RAFAEL SFAIR ^{13,4,14} NICOLAS MORALES ⁵ FRANCOIS COLAS ¹⁵ FRÉDÉRIC VACHIER ⁶
MÓNICA VARA LUBIANO ⁵ RODRIGO BOUFLEUR ³ MERT ACAR ¹⁶ FRANCISCO J. ACEITUNO ^{5,4}
MIGUEL R. ALARCON ^{17,18} SINAN ALIS ^{19,20} SERGIO ALONSO ^{21,22} JAVIER ALONSO-SANTIAGO ²³
FLAVIA AMADIO ²⁴ LAERTE ANDRADE ²⁵ PASCAL ANDRÉ ²⁶ JONATÃ ARCAS-SILVA ^{1,3} ALPER K. ATEŞ ¹⁶
DAVID LAFUENTE AZNAR ²⁷ MICHAEL BACKES ^{28,29} MEHMED NAIM BAGIRAN ³⁰ NELSON BALCAR ²⁷ M. A. BARRY ³¹
KHALID BARKAOUI ^{17,32,33} WOLFGANG BEISKER ³⁴ KIRK BENDER ³⁵ ZOUHAIR BENKHALDOUN ^{36,37,38}
SVETLANA BOEVA ³⁹ EBERHARD H. R. BREDNER ³⁴ RICHARD BUSUTTL ⁴⁰ A. Y. BURDANOV ³³ OSCAR CANALES ²⁷
JAVIER ZARAGOZA-CARDIEL ⁴¹ V. CASANOVA ⁵ MATHEUS LEAL CASTANHEIRA ¹¹ PETER CERAVOLO ⁴²
STEVEN J. CONARD ⁴³ LUCIANO NEGRELLO CORREA ¹¹ DANIEL V. COTTON ⁴⁴ V. S. DHILLON ^{45,17}
SERENA DIAMOND ⁴⁶ VLAD DUMITRESCU ²⁷ JOAN DUNHAM ⁴³ DAVID W. DUNHAM ⁴⁷ CHRISTOPHER L. DUSTON ⁴⁸
ESLAM ELHOSSEINY ⁴⁹ ORHAN ERECE ^{50,51} SILA ERYILMAZ ^{50,51} EMILIO J. FERNANDEZ-GARCÍA ⁵
SULEYMAN FISEK ^{19,20} R. SCOTT FISHER ^{52,53} CLYDE FOSTER ⁵⁴ ERIC FRAPPA ⁵⁵ ANTONIO FRASCA ²³
JONAH FREY ⁴⁶ JOSÉ MARÍA GÓMEZ-LIMÓN GALLARDO ⁵ JOSE LUIS MAESTRE GARCIA ⁵⁶ DAVE GAULT ¹²
KOSMAS GAZEAS ⁵⁷ KAI GETROST ⁴³ MICHAËL GILLON ⁵⁸ ALAN GILMORE ⁵⁹ ROBERT GLASSEY ⁶⁰
BRUCE GOWE ⁶¹ K. D. GREEN ⁶² WILLIAM HANNA ¹² NICHOLAS J. HAIGH ²⁷ DEAN HOOPER ²⁷ KAMIL HORNOCH ⁶³
DRAGANA ILIĆ ^{64,65} CRISTÓVÃO JACQUES ^{66,67} FELIX JANKOWSKY ^{68,69} EMMANUEL JEHIN ⁷⁰ SELAMI KALKAN ⁷¹
ROXANNE KAMIN ⁷² MONIKA K. KAMIŃSKA ⁷³ SHAI KASPI ⁷⁴ J. J. KAVELAARS ^{75,76,77} STEPHEN KERR ¹²
ULRICH KOLB ⁴⁰ RICHARD KOMŽÍK ⁷⁸ DOGAN T. KOSEOGLU ⁵⁰ MIKE KRETLOW ^{68,5}
SANGEETA KUCHIBHOTLA ⁷⁹ JEAN LECACHEUX ⁸⁰ ARNAUD LEROY ⁸¹ ALEXIOS LIAKOS ⁸² LUANA LIBERATO ⁸³
PETER LINDNER ²⁷ S. P. LITTLEFAIR ⁴⁵ JOSE M. MADIEDO ⁵ NATALIO MAÍCAS ⁴¹ MARCIO MALACARNE ^{84,85}
PAUL MALEY ⁴³ JAN MÁNEK ⁸⁶ ANNA MARCINIAK ⁷³ PATRICK MARTINEZ ²⁶ RAMÓN IGLESIAS-MARZOA ⁴¹
GRAEME MCKAY ²⁷ STEVE MESSNER ⁴³ ZDENĚK MORAVEC ⁸⁷ EDUARDO FONSECA MORATO ²
MESSIAS FIDÊNCIO NETO ⁸⁸ JOHN NEWMAN ¹² VADIM NIKITIN ⁴³ RICHARD NOLTHENIUS ³⁵ PETER NOSWORTHY ¹²
MOHAMMAD ODEH ⁸⁹ W. OGLOZA ⁹⁰ SIBEL OTKEN ¹⁹ SACIT ÖZDEMİR ⁹¹ ANDRÁS PÁL ⁹² ASHLEY PENNELL ⁹³
AMAURI PEREIRA ⁹⁴ CARLES PERELLO ^{34,95} JEAN PERKINS ⁴⁴ KONSTANTIN VON POSCHINGER ²⁷ THIAGO DO PRADO ²
THEODOR PRIBULLA ⁷⁸ SOHRAB RAHVAR ⁹⁶ GIOVANA RAMON ¹³ SETH REDFIELD ⁹⁷ CLAUDINE RINNER ²⁷
JEAN-PIERRE RIVET ⁹⁸ JOHANNES ANTUNES NASCIMENTO RODRIGUES ^{2,3} ANTONIO ROMÁN-RECHE ²²
FLAVIA LUANE ROMMEL ^{99,3} T. DE SANTANA ¹⁴ T. SANTANA-ROS ^{100,101} ANTONI SELVA ^{102,34}
CHRISTOPH M. SCHAEFER ¹⁴ ANDREW SCHECK ¹⁰³ CARLES SCHNABEL ^{104,34} OLIVIER SCHREURS ¹⁰⁵
ANDREAS SCHWEIZER ^{34,106,107} M. SERRA-RICART ^{108,17,109} NED SMITH ^{43,110} COLIN SNODGRASS ¹¹¹ EDA SONBAS ¹¹²
A. SOTA ⁵ RAFAEL RIBEIRO DE SOUSA ¹³ FABIO AUGUSTO SPINA ^{2,94} THEODORE SWIFT ⁴³ RÓBERT SZAKÁTS ^{113,114}
ALI TAKEY ⁴⁹ MOHAMMAD F. TALAFHA ¹¹⁵ RAMACHRISNA TEIXEIRA ⁸⁸ ZAHIDE TERZIOĞLU ⁹¹
QIUSHI CHRIS TIAN ^{97,116} VAGELIS TSAMIS ¹¹⁷ EYÜP KAAN ÜLGEN ¹¹⁸ OLIVER VINCE ^{119,120}
MARCOS RINCON VOELZKE ¹²¹ CHRISTIAN WEBER ³⁴ JULIEN DE WIT ³³ AND MICHAL ZEJMO ¹²²

¹ Observatório Nacional/MCTI, R. General José Cristino 77, Rio de Janeiro, RJ 20.921-400, Brasil

² Federal University of Technology - Paraná (PPGFA/UTFPR-Curitiba), Av. Sete de Setembro, 3165, CEP 80230-901 - Curitiba - PR - Brazil

³ Laboratório Interinstitucional de e-Astronomia - LIneA, Av. Pastor Martin Luther King Jr 126, CEP: 20765-000 Rio de Janeiro, RJ, Brasil

⁴ LIRA, CNRS UMR8254, Observatoire de Paris, Université PSL, Sorbonne Université, Université Paris Cité, CY Cergy Paris Université, 92190 Meudon, France

⁵ Instituto de Astrofísica de Andalucía (IAA-CSIC), Glorieta de la Astronomía s/n, 18008 Granada, Spain

⁶ Laboratoire Temps Espace (LTE), Observatoire de Paris, Université PSL, CNRS UMR 8255, Sorbonne Université, LNE, 61 Av. de l'Observatoire, F75014 Paris, France

⁷ Institut Polytechnique des Sciences Avancées IPSA, Ivry-sur-Seine 94200, France

- ⁸ *Universidade Federal do Rio de Janeiro - Observatório do Valongo, Ladeira do Pedro Antonio 43, Rio de Janeiro, RJ 20.080-090, Brasil*
- ⁹ *Universidade Federal de Uberlândia (UFU), Uberlândia, MG, Brasil*
- ¹⁰ *Department of Mathematics, naXys, University of Namur, Rue de Bruzelles 61, Namur 5000, Belgium*
- ¹¹ *Universidade Estadual de Ponta Grossa, Av. General Carlos Cavalcanti - Uvaranas, Ponta Grossa - PR, 84030-000, Brazil*
- ¹² *Trans Tasman Occultation Alliance (TTOA), P.O. Box 3181, Wellington, New Zealand*
- ¹³ *UNESP - São Paulo State University, Grupo de Dinâmica Orbital e Planetologia, Av. Ariberto Pereira da Cunha, 333, Guaratinguetá, 12516-410, SP, Brazil*
- ¹⁴ *Institute for Astronomy and Astrophysics, University of Tübingen, Auf der Morgenstelle 10, 72076 Tübingen*
- ¹⁵ *LESIA, Observatoire de Paris, Université PSL, CNRS, Sorbonne Université, 5 place Jules Janssen, 92190 Meudon, France*
- ¹⁶ *İSTEK Belde Schools Observatory, Rasimağa Sk. No:7 D:4, 34664 Üsküdar/İstanbul Turkey*
- ¹⁷ *Instituto de Astrofísica de Canarias (IAC), C/ Vía Láctea, s/n, E-38205, La Laguna, Spain*
- ¹⁸ *Departamento de Astrofísica, Universidad de La Laguna (ULL), E-38206 La Laguna, Canarias, Spain*
- ¹⁹ *Department of Astronomy and Space Sciences, Faculty of Science, Istanbul University, 34116 Istanbul, Türkiye*
- ²⁰ *Istanbul University Observatory Research and Application Center, Istanbul University, 34116 Istanbul, Türkiye*
- ²¹ *Dept. Of Software Engineering, University of Granada, Escuela Técnica Superior de Ingenierías Informática y de Telecomunicación, Calle Periodista Daniel Saucedo Aranda s/n, E-18071 (Granada-Spain)*
- ²² *Sociedad Astronómica Granadina (SAG)*
- ²³ *INAF - Osservatorio Astrofisico di Catania, via S. Sofia 78, 95123 Catania, Italy*
- ²⁴ *Niels Bohr Institute, Jagtvej 155A, 2200 Copenhagen N, Denmark*
- ²⁵ *Laboratório Nacional de Astrofísica, R. Estados Unidos 154, Itajubá, MG, 37504-364, Brazil*
- ²⁶ *ADAGIO, Bélesta Observatory, 31540 Bélesta, France*
- ²⁷ *Lucky Star Observer Colaborator*
- ²⁸ *Department of Physics, Chemistry & Material Science, University of Namibia, 340 Mandume Ndemufayo Avenue, Private Bag 13301, Windhoek, Namibia*
- ²⁹ *Centre for Space Research, North-West University, Private Bag X6001, Potchefstroom 2520, South Africa*
- ³⁰ *TURKSAT*
- ³¹ *Linden Observatory, Glossop Rd., Linden, NSW 2778 AUS*
- ³² *Astrobiology Research Unit, Université de Liège, Allée du 6 Août 19C, B-4000 Liège, Belgium*
- ³³ *Department of Earth, Atmospheric and Planetary Science, Massachusetts Institute of Technology, 77 Massachusetts Avenue, Cambridge, MA 02139, USA*
- ³⁴ *International Occultation Timing Association / European Section e.V. (IOTA/ES), Am Brombeerhag 13, 30459 Hannover, Germany*
- ³⁵ *Departament of Astronomy, Cabrillo College, 6500 Soquel Dr Aptos, CA 95003, USA*
- ³⁶ *Department of Applied Physics and Astronomy, University of Sharjah, United Arab Emirates.*
- ³⁷ *Sharjah Academy for Astronomy, Space Sciences and Technology, University of Sharjah, United Arab Emirates*
- ³⁸ *Oukaimeden Observatory, High Energy Physics, Astrophysics and Geoscience Laboratory, FSSM, Cadi Ayyad University, Marrakesh, Morocco.*
- ³⁹ *Institute of Astronomy and NAO, Bulgarian Academy of Sciences, 72 Tsarigradsko 5 Chaussee Blvd., 1784 Sofia, Bulgaria*
- ⁴⁰ *Faculty of Science, Technology, Engineering & Mathematics, The Open University, Walton Hall, Milton Keynes MK7 6AA, UK*
- ⁴¹ *Centro de Estudios de Física del Cosmos de Aragón (CEFCA), Plaza San Juan 1, 44001 Teruel, Spain*
- ⁴² *Anarchist Mt. Observatory, British Columbia, Canada*
- ⁴³ *International Occultation Timing Association, (IOTA-US), 2760 SW Jewell Ave, Topeka, Kansas, USA*
- ⁴⁴ *Monterey Institute for Research in Astronomy, 200 8th St., Marina, California, USA*
- ⁴⁵ *Astrophysics Research Cluster, School of Mathematical and Physical Sciences, University of Sheffield, Sheffield, S3 7RH, UK*
- ⁴⁶ *Westport Astronomical Society, 182 Bayberry Lane, Westport, CT 06880, USA*
- ⁴⁷ *KinetX, Inc. Space Navigation and Flight Dynamics Practice*
- ⁴⁸ *Merrimack College, N Andover, MA, 01845, USA*
- ⁴⁹ *National Research Institute of Astronomy and Geophysics (NRIAG), 11421 Helwan, Cairo, Egypt*
- ⁵⁰ *Türkiye National Observatories, TUG, 07070, Antalya, Türkiye*
- ⁵¹ *Scientific and Technological Research Council of Türkiye (TÜBİTAK), 06680, Ankara, Türkiye*
- ⁵² *University of Oregon, Department of Physics*
- ⁵³ *Pine Mountain Observatory*
- ⁵⁴ *Astronomical Society of Southern Africa*
- ⁵⁵ *Euraster, 8 rue du tonnelier 46100 Faycelles, France.*
- ⁵⁶ *Observatorio de Albox - Almeria (MPC Z90)*
- ⁵⁷ *Section of Astrophysics, Astronomy and Mechanics, Department of Physics, National and Kapodistrian University of Athens, GR-15784 Zografos, Athens, Greece*
- ⁵⁸ *Astrobiology Research Unit, Université de Liège, Allée du 6 août 19, Liège 4000, Belgium*
- ⁵⁹ *University of Canterbury Mt John Observatory*

- ⁶⁰ *Canterbury Astronomical Society, 218 Bells Road, West Melton 7671, Canterbury, New Zealand*
- ⁶¹ *Penticton Secondary School, 158 Eckhardt Ave E, Penticton BC, Canada*
- ⁶² *University of New Haven, West Haven, CT 06516 USA*
- ⁶³ *Astronomical Institute of the Czech Academy of Sciences, Fričova 298, CZ-251 65 Ondřejov, Czech Republic*
- ⁶⁴ *Department of Astronomy, Faculty of Mathematics, University of Belgrade, Studentski trg 16, 11000 Belgrade, Serbia*
- ⁶⁵ *Hamburger Sternwarte, Universität Hamburg, Gojenbergsweg 112, D-21029 Hamburg, Germany*
- ⁶⁶ *SONEAR Observatory – CEAMIG, Caeté, Minas Gerais, Brazil*
- ⁶⁷ *Centro de Estudos Astronômicos de Minas Gerais (CEAMIG), Belo Horizonte, Brazil*
- ⁶⁸ *German Center for Astrophysics (DZA), Postplatz 1, 02826 Görlitz, Germany*
- ⁶⁹ *Heidelberg State Observatory (LSW), Königstuhl 12, 69117 Heidelberg, Germany*
- ⁷⁰ *Space Sciences, Technologies and Astrophysics Research (STAR) Institute, University of Liège, Liège, Belgium*
- ⁷¹ *Ondokuz Mayıs University Observatory Samsun/Türkiye*
- ⁷² *Naylor Observatory, Lewisberry, PA*
- ⁷³ *Astronomical Observatory Institute, Faculty of Physics and Astronomy, Adam Mickiewicz University, ul. Słoneczna 36, 60-286 Poznan, Poland*
- ⁷⁴ *School of Physics and Astronomy and Wise Observatory, Tel Aviv University, Tel Aviv 6997801, Israel*
- ⁷⁵ *National Research Council of Canada, Herzberg Astronomy and Astrophysics Research Centre, 5071 W. Saanich Rd. Victoria, BC, V9E 2E7, Canada*
- ⁷⁶ *Department of Physics and Astronomy, University of Victoria, Elliott Building, 3800 Finnerty Road, Victoria, BC V8P 5C2, Canada*
- ⁷⁷ *Department of Physics & Astronomy, University of British Columbia, 6224 Agricultural Road, Vancouver, BC V6T 1Z1, Canada*
- ⁷⁸ *Astronomical Institute, Slovak Academy of Sciences, 059 60 Tatranská Lomnica, Slovakia*
- ⁷⁹ *John J. McCarthy Observatory, 388 Danbury Rd, New Milford, CT 06776, USA*
- ⁸⁰ *Meudon Observatory, 5 Place Janssen, 92190-Meudon, France*
- ⁸¹ *Uranoscope de l'Île de France, Allée Camille Flammarion 77220 Gretz-Armainvilliers, France - Planète Sciences, 10 rue du Marquis de Raies, 91080 Evry-Courcouronnes, France*
- ⁸² *Institute for Astronomy, Astrophysics, Space Applications & Remote Sensing, National Observatory of Athens, I. Metaxa & Pavlou St., GR15236, Athens, Greece*
- ⁸³ *Université Côte d'Azur, Observatoire de la Côte d'Azur, CNRS, Laboratoire Lagrange, Bd de l'Observatoire, CS 34229, 06304 Nice Cedex 4, France*
- ⁸⁴ *Universidade Federal do Espírito Santo (UFES), Av. Fernando Ferrari, 514, Campus Universitário de Goiabeiras, Vitória, Espírito Santo – CEP 29.075.910*
- ⁸⁵ *Instituto Nacional de Pesquisas Espaciais (INPE), Av. dos Astronautas, 1758, Jardim da Granja, São José dos Campos - SP, CEP 12227-010*
- ⁸⁶ *Czech Astronomical Society (Occultation Section)*
- ⁸⁷ *Observatory and Planetarium Teplice, Kopernikova 3062, 415 01 Teplice, Czech Republic*
- ⁸⁸ *Observatório Abrahão de Moraes - Instituto de Astronomia Geofísica e Ciências Atmosféricas - USP. Rua do Matão 1226 Cidade Universitária, São Paulo - SP.*
- ⁸⁹ *International Astronomical Center (IAC), Al-Khatim Observatory, Abu Dhabi, United Arab Emirates*
- ⁹⁰ *University of National Education Commission*
- ⁹¹ *Department of Astronomy and Space Sciences, Ankara University, Science Faculty, Tandoğan, Ankara, 06100, Turkey*
- ⁹² *Konkoly Observatory, HUN-REN CSFK, MTA Centre of Excellence, Konkoly Thege M. út 15-17, Budapest, 1121, Hungary*
- ⁹³ *Dunedin Astronomical Societies Beverly Begg Observatory IAU R58*
- ⁹⁴ *Colégio Estadual do Paraná (CEP), Av. João Gualberto, 250 - Centro, Curitiba - PR, 80030-000*
- ⁹⁵ *Agrupació Astronòmica de Sabadell, Carrer Prat de la Riba s/n, Sabadell, ES*
- ⁹⁶ *Perimeter Institute for Theoretical Physics, Waterloo, ON N2L 2Y5, Canada*
- ⁹⁷ *Astronomy Department and Van Vleck Observatory, Wesleyan University, 96 Foss Hill Drive, Middletown, CT 06459, USA*
- ⁹⁸ *Université Côte d'Azur, Observatoire de la Côte d'Azur, CNRS, Laboratoire Lagrange, France*
- ⁹⁹ *Florida Space Institute, University of Central Florida, 12354 Research Parkway, Partnership I, Room 211, 32826 Orlando, USA.*
- ¹⁰⁰ *Departamento de Física, Ingeniería de Sistemas y Teoría de la Señal, Universidad de Alicante, Carr. San Vicente del Raspeig, s/n, 03690 San Vicente del Raspeig, Alicante, Spain*
- ¹⁰¹ *Institut de Ciències del Cosmos (ICCUB), Universitat de Barcelona (UB), c. Martí Franquès, 1, 08028 Barcelona, Catalonia, Spain*
- ¹⁰² *Centre Astronòmic del Pedraforca (CAP), Saldes, Spain*
- ¹⁰³ *International Occultation Timing Association, Fountain Hills, AZ 85269, USA*
- ¹⁰⁴ *Agrupació Astronòmica de Sabadell*
- ¹⁰⁵ *Observatoire de Nandrin, Société Astronomique de Liège, Belgium*
- ¹⁰⁶ *Stellar Occultation Timing Association Switzerland (SOTAS)*
- ¹⁰⁷ *Sternwarte Büllach Observatory, MPC 167*

- ¹⁰⁸*Light Bridges, SL. Observatorio Astronómico del Teide. Carretera del Observatorio del Teide, s/n, Güímar, Santa Cruz de Tenerife, Spain*
- ¹⁰⁹*Departamento de Astrofísica, Universidad de La Laguna, Avda. Astrofísico Francisco Sánchez, 38206 La Laguna, Tenerife, Spain*
- ¹¹⁰*Barnard Astronomical Society, Chattanooga, TN*
- ¹¹¹*Institute for Astronomy, University of Edinburgh, Royal Observatory, Edinburgh EH9 3HJ, UK*
- ¹¹²*Department of Physics, The George Washington University, Washington, DC 20052, USA*
- ¹¹³*HUN-REN Research Centre for Astronomy and Earth Sciences, Konkoly Observatory, Konkoly Thege Miklós út 15-17., H-1121 Budapest, Hungary*
- ¹¹⁴*Research Centre for Astronomy and Earth Sciences, MTA Centre of Excellence, Konkoly Thege Miklós út 15-17., H-1121 Budapest, Hungary*
- ¹¹⁵*Universty of Sharjah, Sharjah Academy of Astronomy, Space Sciences and Technology, SAASST, Sharjah City, Sharjah, 27272, United Arab Emirates*
- ¹¹⁶*Leiden Observatory, Leiden University, P.O. Box 9513, 2300 RA Leiden, The Netherlands*
- ¹¹⁷*Sparta Astronomy Association, Amyklon 22, 15231 Halandri, Greece*
- ¹¹⁸*Huawei Türkiye Ar-Ge Merkezi, 34768, İstanbul, Türkiye*
- ¹¹⁹*Astronomical Observatory, Volgina 7, 11060 Belgrade, Serbia*
- ¹²⁰*Shanghai Astronomical Observatory, Chinese Academy of Sciences, 80 Nandan Road, Shanghai 200030, People's Republic of China*
- ¹²¹*Cruzeiro do Sul University, R. Galvao Bueno 868, Sao Paulo, SP, 01506-000, Brazil*
- ¹²²*Janusz Gil Institute of Astronomy University of Zielona Gora, Poland*

ABSTRACT

We present results from 28 stellar occultations by the large Trans-Neptunian Object (50000) Quaoar registered between 2018 and 2025. By performing a joint analysis of this occultation data-set, along with other 9 published events, we were able to fit an oblate ellipsoid shape, with equatorial semi-axes, a and b of $566.1_{-2.2}^{+2.5}$ km, and a polar semi-axis, c , of $511.2_{-3.7}^{+3.6}$ km. It provides an equivalent volumetric diameter of 1094.4 ± 4.6 km and polar oblateness of 0.097 ± 0.011 . Considering an absolute magnitude of $H = 2.79 \pm 0.35$, we derive a geometric albedo of $p_V = 0.125 \pm 0.038$. We have derived new upper limits to the surface pressure of a CH_4 atmosphere of 0.15 nbar (1σ) and 0.65 nbar (3σ). We also provide a table with the 36 new astrometric positions for Quaoar. Using the new system mass derived from Weywot's orbit around Quaoar, we calculated a density of 1.760 ± 0.109 g/cm³. Moreover, from the derived size and rotation period (8.8394 ± 0.0002 hours (Ortiz et al. 2003)), we calculate that, if Quaoar is in Maclaurin hydrostatic equilibrium state, it would have a density of 1.859 ± 0.200 g/cm³. This result, within the error bars, is compatible with the value we found. Therefore, this work shows that Quaoar can be a Maclaurin object, being eligible as a dwarf planet.

Keywords: Quaoar — trans-Neptunian Object — Stellar occultation — Maclaurin equilibrium

1. INTRODUCTION

Since the first stellar occultation by (50000) Quaoar observed in 2011 (Person et al. 2011; Braga-Ribas et al. 2013), knowledge about this object has steadily increased. In total, Quaoar's shadow has been detected during 36 distinct stellar occultation events, though only restricted analysis of 13 of these events have been published so far (see Table 1). Furthermore, two rings outside the Roche Limit were found around Quaoar (Morgado et al. 2023; Pereira et al. 2023).

A stellar occultation occurs when a solar system object passes in front of a background star, temporarily blocking its light and casting a shadow at a given location. Each observational detection of the object's shadow at different points on the ground provides a positive chord (i.e., a unidimensional measurement of

its profile), while non-detections are called negative chords and can constrain the object's size and position (when associated with positive detections) (Sicardy et al. 2024).

In this work, we present 83 new positive chords for Quaoar, out of a total dataset of 107 positive chords, not counting additional observations made with instruments that simultaneously acquired data in multiple filters. This extensive set of occultations over diverse epochs allows for a comprehensive analysis of the global properties of Quaoar, such as those made for Chariklo (Leiva et al. 2017; Morgado et al. 2021), 2002 KX₁₄ (Rizos et al. 2025), 2003 AZ₈₄ (Dias-Oliveira et al. 2017) and others.

Quaoar is one of the largest Trans-Neptunian Objects (TNOs) known to date. Because it is not in mean motion resonance with Neptune, Quaoar is clas-

sified as a classical Kuiper belt object, and its orbital inclination ($>8^\circ$) places it among the dynamically hot population (Lykawka & Mukai 2007). The first multi-chord stellar occultation by Quaoar reported by Braga-Ribas et al. (2013) derived an equivalent diameter of $1,110 \pm 5$ km, assuming a Maclaurin spheroid shape with equatorial radius 572.5 ± 20.5 km and polar oblateness of 0.0917 ± 0.0222 . In 2022, a ten-chord occultation reported by Pereira et al. (2023) produced a sky-plane ellipse fit with semi-major axis 579.5 ± 4.0 km and apparent flattening 0.12 ± 0.01 , consistent with Braga-Ribas et al. (2013) projection. Finally, Kiss et al. (2024) combined Braga-Ribas et al. (2013) occultation data with K2 photometry and Herschel PACS thermal light curves to obtain an equivalent diameter of $1,090 \pm 40$ km.

Weywot, Quaoar’s known satellite, was discovered in 2007 (Brown & Suer 2007), and its first orbit determinations were given by Vachier et al. (2012) and Fraser et al. (2013). Using four stellar occultations by Weywot, Braga-Ribas et al. (2025) derived precise relative positions, which were used to improve its orbital parameters and derive the system mass ($1.208 \pm 0.063 \times 10^{21}$ kg). Weywot orbits Quaoar at a distance of $13,309 \pm 231$ km, with an eccentricity of 0.018 ± 0.016 and an orbital inclination relative to the Ecliptic of $38.0^\circ \pm 1.4^\circ$, yielding an orbital period of 12.431013 ± 0.00021 days. Braga-Ribas et al. (2025) have also determined Weywot’s orbital pole as $\alpha_W: 266.9^\circ \pm 1.5^\circ$ and $\delta_W: 51.9^\circ \pm 1.4^\circ$.

Additionally, as mentioned, Quaoar possesses two known rings (Morgado et al. 2023; Pereira et al. 2023). More recently, a new opaque structure has been detected at a distance of $5,700$ km from the main body center, indicating that more material is present around it (Nolthenius et al. 2025). The outer ring (QR1) orbits Quaoar at a distance of $4,057 \pm 5$ km, with its pole orientation given by $\alpha_{QR}: 259.82 \pm 0.23^\circ$ and $\delta_{QR}: 53.45 \pm 0.3^\circ$ (Pereira et al. 2023), and the inner (QR2) at $2,520 \pm 20$ km, with the same pole. There is a small discrepancy between the orientation of Quaoar’s ring system (Pereira et al. 2023) and Weywot’s orbit (Braga-Ribas et al. 2025), causing an inclination between the two orbital planes of $4.8 \pm 1.4^\circ$.

There is no current evidence indicating that Weywot significantly interferes with the stability of Quaoar’s rings. Therefore, its orbital inclination is consistent with current ring models (Rodríguez et al. 2023). Nevertheless, studies by the authors of this paper are currently underway to verify if Weywot and its orbital characteristics are related to Quaoar’s 3D shape, and whether it could influence the object’s figure, potentially leading to a specific triaxial configuration (Margoti 2024). Ring

systems are generally expected to orbit along the equatorial plane of their central bodies; therefore, Quaoar and its rings are assumed to share the same pole orientation. We used this assumption to derive Quaoar’s three-dimensional shape in this work.

For objects the size of Quaoar, it is expected that they presented an atmosphere at some point in their formation history (Sicardy 2023). Stellar occultation light curves have been used to determine the current 1σ atmospheric limits for Quaoar, which are: 21 nbar (Braga-Ribas et al. 2013), 6 nbar (Arimatsu et al. 2019), 85 nbar (Morgado et al. 2022), and 0.2 nbar (Proudfoot et al. 2025).

Specifically, using the measured chords, we investigated the dimensions of Quaoar assuming it to be an oblate spheroid, assessed whether it could be in Maclaurin hydrostatic equilibrium, and compared our results with those obtained by Braga-Ribas et al. (2013). For the latter purpose, a rotation period is also necessary. Ortiz et al. (2003) proposed two rotation periods for Quaoar: 8.8394 ± 0.0002 hours if Quaoar’s rotational light curve is single-peaked (implying an oblate shape), and 17.6788 ± 0.0004 hours if it is double-peaked (indicating a triaxial shape). Kiss et al. (2024) also proposed similar rotation periods: 8.8364 ± 0.0031 hours for an oblate shape, and 17.6728 ± 0.0062 hours for a triaxial shape. The main issue with adopting an oblate shape is that the entire amplitude of Quaoar’s rotational light curve would then have to be explained solely by albedo variegation, which has amplitudes of 0.133 ± 0.028 mag according to Ortiz et al. (2003), and 0.154 ± 0.040 mag according to Kiss et al. (2024).

This paper presents the results of the analysis of new stellar occultations by the large Trans-Neptunian Object (50000) Quaoar, registered between 2018 and 2025. Following this introduction, Section 2 details the predictions and observational campaigns that provided the data for this work. Section 3 describes the analysis of the data, including the occultation light curves, the fitting of an oblate ellipsoid model to determine Quaoar’s shape, and we establish a limit on Quaoar’s atmosphere. Finally, in Section 4, we present our conclusions, discussing the implications of our findings for Quaoar’s density and its potential to be classified as a dwarf planet. The Appendix provides additional details regarding the stellar information (Appendix A), observer information (Appendix D), figures of the light curves (Appendix B) and new astrometric position for Quaoar (Appendix C).

2. PREDICTIONS AND CAMPAIGNS

Predicting a stellar occultation requires the sky position of the occulting body over time (its ephemeris)

and the occulted star’s apparent position (as seen by a given observer). Both should be known to within a few tens of milliarcseconds (*mas*) (Sicardy et al. 2024), on the order of the object’s own angular size in the sky (around 50 mas in the case of Quaoar), for having a precise prediction (Braga-Ribas et al. 2013).

In this work, we present 28 new stellar occultations by Quaoar that occurred between 2018 and 2025. These events were predicted within the Lucky-Star Collaboration¹. The Lucky-Star Collaboration aims to provide reliable stellar occultation predictions to enhance our understanding of solar system objects. To achieve this, the ephemerides of a select list of TNOs, Centaurs, and Trojans are frequently updated using *NIMA* integrator (Desmars et al. 2015) with astrometric data from recurring observations, obtained from our own observations and analysis (Assafin 2023a); information is publicly available on the Lucky-Star website². Moreover, occultation events themselves produce astrometric positions with uncertainties on the order of fractions of *mas*, which are also used to refine the ephemerides (Rommel et al. 2020). All events analyzed in this work were predicted using stars from the GAIA DR2 and DR3 catalogs (Gaia Collaboration et al. 2018, 2021). Details on the occultation stars’ information, along with their propagated positions to the event date, are shown in the Appendix A, Table 3.

The occultation data were acquired using a wide range of telescopes, from those with large apertures, such as Gran Telescopio Canarias (GTC, 10.4 m), the Gemini North (8.0 m), and the Southern Astrophysical Research Telescope (SOAR, 4.1 m), to apertures smaller than 60 centimeters. The majority of observations were carried out by small observatories and citizen scientists around the world (e.g., IOTA members³). In addition to the diverse range of telescopes, a wide array of instruments was also used, such as the HiPERCAM (Dhillon et al. 2021) at GTC and SPARC4 (Bernardes et al. 2025) at Observatório Pico dos Dias (OPD), which enabled simultaneous image acquisition in multiple channels, to CMOS and video detectors such as the QHY174M-GPS and Watec 910BD models, on mobile telescopes.

All stellar occultation events for which Quaoar’s shadow was detected are summarized in Table 1. Details on the locations, telescope, camera, exposure time, and cycle are provided in the Appendix D, Tables 5 and 6. A subset of events the events in Table 1 overlapped with

this work has been published previously, but those studies focused exclusively on Quaoar’s ring or Weywot detections rather than the primary body itself.

Since 2022, the Lucky Star’s Occultation Portal (Kilic et al. 2022) has been used to store the occultation data, including events by Quaoar. This has greatly streamlined the organization of observer information, data backups, distribution, and long-term studies like this work. Therefore, from 2022 on, the reports and data related to Quaoar occultations were collected using the Occultation Portal⁴.

3. ANALYSIS

This section is dedicated to explaining the methodology utilized to analyze the data obtained from the stellar occultations. Specifically, Section 3.1 details the procedures for obtaining the occultation light curves, Section 3.2 covers the fitting of the oblate model, and Section 3.3 describes our atmosphere fitting analysis.

3.1. Occultation light curves

The variety file formats was as diverse as the variety of telescopes and cameras. The most common format was FITS (Hanisch et al. 2001), although video sequences in formats such as AVI, SER⁵, AAV⁶, ADV (Pavlov et al. 2020) and H5⁷ were also present. When images were supplied in a format other than FITS, they were first converted to FITS using custom Python software based on the `numpy` (Harris et al. 2020) and `astropy` (Astropy Collaboration et al. 2022) libraries.

When calibration images were provided, bias (or darks) and flats, the science images were calibrated accordingly. In some cases, additional calibration was necessary by dividing each pixel by the mean of its corresponding row or column. This step was required because cameras such as the Watec and QHY174M-GPS, and colour sensors, often exhibit line-by-line (or column-by-column) noise that varies from frame to frame, and normalizing each pixel by the average of its row (or column) effectively suppressed this systematic effect.

For video files like AVI, acquired from analog cameras, images are recorded with a fixed minimum exposure time of 0.040 s, which corresponds to the exposure

¹ Lucky-Star Collaboration: <https://lesia.obspm.fr/lucky-star/team.php>

² Website: <https://lesia.obspm.fr/lucky-star/nima.php>

³ International Occultation Timing Association

⁴ Occultation Portal: <https://opop.obspm.fr/>

⁵ Documentation: <https://siril.readthedocs.io/en/latest/file-formats/SER.html>

⁶ Documentation: <http://www.hristopavlov.net/OccuRec/AavFormat.html>

⁷ Documentation: <https://support.hdfgroup.org/documentation/hdf5/latest/>

Table 1. Summary of Stellar Occultation Events by Quaoar. The columns are as follows: Event (the date of the occultation); P: Positive (the number of positive chords detected), N: Negative (the number of negative chords), and O: Other (observations that did not yield conclusive data due to technical issues, poor weather, or inconclusive photometry); and reference. The symbols are used to indicate specific types of detections: an star (*) represents a QR1 detection; two stars (***) indicate QR1 and QR2 detections; a bullet point (•) symbolizes a positive chord observed by a space telescope; a dagger (†) marks the detection of both Quaoar and Weywot; and a double dagger ‡ marks the detection of a possible double star.

Event	P / N / O	Reference
2011-02-11	2 / 0 / 0	Person et al. (2011) This Work
2011-05-04	6 / 9 / 1	Braga-Ribas et al. (2013)
2012-02-17	4 / 0 / 0	Braga-Ribas et al. (2013)
2012-10-15	1 / 0 / 3	Braga-Ribas et al. (2013)
2013-07-09	1 / 0 / 0	Rommel et al. (2020)
2018-07-26	4 / 0 / 0	This Work
2018-09-02*‡	1 / 0 / 0	Morgado et al. (2023) This Work
2019-03-27	1 / 0 / 0	This Work
2019-04-28	2 / 0 / 0	This Work
2019-05-28	4 / 0 / 10	This Work
2019-06-05	5 / 0 / 0	Morgado et al. (2023) This Work
2019-06-28	1 / 0 / 3	Arimatsu et al. (2019)
2019-08-04†	1 / 0 / 0	Braga-Ribas et al. (2025) This Work
2019-09-26	4 / 0 / 0	This Work
2019-10-16	3 / 0 / 0	This Work
2020-06-11*•	1 / 1 / 0	Morgado et al. (2022)
2020-06-16	4 / 0 / 0	This Work
2020-07-01	1 / 1 / 0	This Work
2022-06-24	1 / 0 / 0	This Work
2022-08-09***	10 / 1 / 19	Pereira et al. (2023)
2023-05-13	4 / 1 / 10	This Work
2023-05-20*	1 / 0 / 0	This Work
2023-05-24*	1 / 4 / 0	This Work
2023-05-26†	4 / 4 / 2	Braga-Ribas et al. (2025) This Work
2023-07-15	7 / 0 / 13	This Work
2023-08-01	4 / 0 / 1	This Work
2023-08-24	5 / 0 / 5	This Work
2024-04-10**	5 / 0 / 3	This Work
2024-05-29	1 / 0 / 0	This Work
2024-07-04*	7 / 1 / 3	This Work
2024-08-28* * •	1 / 0 / 0	Proudfoot et al. (2025)
2025-06-12*	3 / 2 / 1	This Work
2025-06-20	6 / 0 / 7	This Work
2025-07-04*	1 / 1 / 4	This Work
2025-08-28‡	2 / 1 / 1	This Work
2025-08-31	2 / 0 / 1	This Work

time of an individual extracted frame in Phase Alternating Line (PAL) mode. Consequently, the science images had to be stacked to achieve the actual exposure time, which is a multiple of this minimum value. In addition, video acquisitions are typically accompanied by timestamps written in the image, which requires extracting these timestamps for each frame.

Furthermore, cameras like the Watec and Raptor require specific time corrections (Barry et al. 2015). For the Watec cameras, the corrections are indicated in publicly available tables⁸. The Raptor Merlin camera records, on its header, the computer time at 1.5 exposure intervals after the actual image’s mid-acquisition time. All these corrections were already applied in the event instants shown in Table 6.

The vast majority of the instruments used in the Quaoar observation campaigns were equipped with GPS antennas for time calibration. In the case of Raptor cameras, the acquisition start time is retrieved from the control computer and recorded in the FITS headers, while QHY cameras retrieve timing directly from an internal GPS. Observers who did not have access to GPS-based acquisition utilized the Network Time Protocol (NTP) most suitable for their observatory. Although this protocol is less reliable than a dedicated GPS antenna, such chords were allowed to undergo time shifts to align them with the GPS-timed chords. Since a regular shape for Quaoar is a physical prior, the alignment of these chords is a natural consequence of the modeling process. In our campaigns, only one observatory utilized neither a GPS antenna nor an NTP protocol. This specific chord, indicated in Table 6, exhibited a significant initial offset; therefore, a random offset was applied to center it with the remaining chords.

Combining occultation data from dozens of distinct observational setups naturally introduces non-trivial systematic timing uncertainties and cross-calibration issues. While internal random errors are derived directly from light curve pipeline fittings, the absolute time anchoring depends heavily on the synchronization method utilized, such as dedicated GPS, various NTP protocols, or internal computer clocks. To mitigate these potential cross-calibration offsets, chords backed by absolute GPS timing were used as anchors for each specific event. Chords obtained via less reliable protocols (e.g., NTP) or those presenting known systematic instrumentation delays were allowed to undergo time shifts. This alignment procedure is physically justified by adopting

⁸ Website: http://www.dangl.at/ausruet/vid_tim/vid_tim1.htm#wat_910bd

a regular shape for Quaoar as a physical prior for individual single-epoch projections. Consequently, while individual instrumentation combinations present systematic footprints, our cross-calibration framework absorbs these misaligned chords before feeding the dataset into the global shape optimization.

This multi-epoch dataset is strongly heteroskedastic, combining observations from telescopes ranging in aperture from 10.4 m down to 30 mm. To prevent individual, highly precise chords from dominating the global solution, and to account for residual cross-calibration timing offsets across distinct equipment, our optimization relies on the systematic uncertainty floor $\sigma_{model} = 2$ km defined in Equation 1. This parameter acts as an empirical weighting factor across the network: by enforcing a reduced χ_{pdf}^2 close to unity, the MCMC exploration naturally inflates the posterior probability contours. Consequently, the derived parameter uncertainties (Table 2) effectively incorporate both the random noise of individual chords and the underlying instrumentation cross-calibration scatter.

Differential aperture photometry of each dataset was primarily obtained with the Platform for Reduction of Astronomical Images Automatically PRAIA (Assafin 2023b). For datasets requiring extra care due to issues like undersampling of the target star (i.e., SNR less than 1.5), we employed our custom Python code. This code automatically detects the field and uses a genetic algorithm to determine the optimal centroid and aperture for each star in the photometry, particularly for the occultation target. It is based on `numpy` and `astropy`, and also utilizes `astrometry.net`, `scikit-learn` (Peregrina et al. 2011), and `deap` (Fortin et al. 2012).

All photometric data for the positive chords obtained in this work are organized by year in the Appendix B, Figures 4 to 6. The occultation timings for each of these light curves were determined using our custom reduction pipeline based on the Python library SORA (Gomes-Júnior et al. 2022); the timings for each chord are listed in Table 6. Finally, the projection of the chords onto the plane of the sky was also performed with SORA using Quaoar ephemerides NIMAv19⁹ and planetary ephemeris DE442, the chords are shown in Figure 2.

3.2. Oblate fitting and uncertainty determination

Considering the predicted diameter for Quaoar and its composition of rock and ice (Braga-Ribas et al. 2013), it is reasonable to assume that it is in hydrostatic equilib-

rium, and the simplest equilibrium figure is that of an oblate spheroid (Tancredi & Favre 2008).

Since 2011, Quaoar has been the target of 36 successful stellar occultations. Using these occultations, we aimed to employ an oblate model to represent all the observed chords.

The fitting of the oblate model to the observational data was performed through a bayesian statistical inference approach, using the Markov Chain Monte Carlo (MCMC) method. The goal was not only to find the best-fit set of parameters but also to map the posterior probability distribution to characterize the uncertainties and correlations among all the model’s variables.

The geometric model of the oblate ellipsoid has four global parameters: the equatorial semi-axes $a = b$, the rotational polar-axis c , and the orientation, described by the right ascension (α_Q) and declination (δ_Q) of its rotation axis. In addition, the model was fitted to the 36 data sets from the different occultations, requiring 70 additional parameters related to the projected center coordinates of the ellipsoid (f_i, g_i , for $i=1, \dots, 36$). This resulted in a total of 76 parameters to be determined.

The quality of the fit for each occultation set was quantified by a chi-squared (χ^2) test. The final χ^2 was obtained by summing the individual χ^2 values from each occultation, according to the equation:

$$\chi^2 = \sum_{i=1}^N \frac{(r_i - r'_i)^2}{\sigma_i^2 + \sigma_{model}^2}, \quad (1)$$

where r_i is the radial distance of the i th observed chord extremity, r'_i is the radial distance of the ellipsoid shadow limb, σ_i is the observed radial uncertainty at each extremity, and σ_{model} represents the uncertainty in our ellipsoidal model relative to Quaoar’s 3D shape (for example, due to topographic features (Rommel et al. 2025)). We iteratively estimated σ_{model} as 2 km, ensuring that χ^2 per degree of freedom remains close to 1.

The uncertainties quoted for our final solutions, presented in Table 2, provide a robust assessment of our model constrained to an oblate object. Combining 14 years of multi-epoch data across distinct geometries and variety of equipment requires accounting for localized topographic features or systemic discrepancies, especially in the chord timings, which are critical to shape determination. This population of possible true variations is encapsulated in our framework via the introduction of the $\sigma_{model} = 2$ km parameter in Equation 1. Rather than enforcing an uncalibrated weight on high-dispersion or over-precise chords, this baseline systematic error acts as an absolute uncertainty floor applied in the direction of every single chord extremity. The physical magnitude of this floor (2 km) was systemat-

⁹ The ephemeris is available at the following link: <https://lesia.obspm.fr/lucky-star/obj.php?p=1177>

ically cross-evaluated against expected global topography bounds derived from [Johnson & McGetchin \(1973\)](#) using the results from [Braga-Ribas et al. \(2013\)](#). By ensuring our final MCMC joint probability exploration yields a minimum $\chi_{pdf}^2 = 0.998$ close to unity, the calculated marginal distributions inherently incorporate both the statistical observational noise and the underlying systematic profile dispersion, providing representative true uncertainty values for the oblate model.

For the analysis, we first assumed that Quaoar’s pole orientation is aligned with that of its rings ($\alpha_Q = \alpha_{QR} = 259.82 \pm 0.23^\circ$ and $\delta_Q = \delta_{QR} = 53.45 \pm 0.30^\circ$ [Pereira et al. \(2023\)](#)), which helped constrain the range of possible solutions. By modeling the object as an oblate spheroid with no pole precession, we ensure the pole’s orientation remains constant. The only variation in the projection of its limb, therefore, is caused by the changing aspect angle, which is unrelated to the object’s rotational phase. This allows us to disregard the object’s rotation period and initial phase.

To optimize the fitting process and deal with the dependent nature of the local parameters (f_i, g_i), a profile likelihood analysis method was employed. For each set of global parameters (a, c, α_{QR} and δ_{QR}) sampled by the MCMC, the optimal values of the projected centers (f_i, g_i) were determined by a minimization for each of the 36 dates. This procedure ensures that the χ^2 evaluation for each point in the global parameter space represents the best possible fit, incorporating the uncertainties of the local parameters into the uncertainty analysis of the global parameters.

The MCMC algorithm was used to explore the 76-dimensional space and generate a long chain of samples (points), whose density is proportional to the posterior probability function.

The uncertainties for the parameters were obtained from this posterior probability distribution. The marginal probability distributions for each parameter were constructed from histograms of the sample chain. The best-fit value for each variable was considered the median of its respective distribution, and the 1σ uncertainties (68.3% confidence interval) were determined by the 16th and 84th percentiles of the distribution.

The correlations among the parameters and the shape of the marginal and joint probability distributions can be visualized in the corner plot, figure 1, which displays all the histograms and two-dimensional projections of the posterior probability distribution.

This resulted the semi-axis and pole-position, with the respective uncertainties, which best represent the 36 observed events, being: $a = b = 566.1_{-2.2}^{+2.5}$ km, $c = 511.2_{-3.7}^{+3.6}$ km, $\alpha_Q = 259.7_{-0.2}^{+0.2} \circ$ and $\delta_Q = 53.4_{-0.2}^{+0.2} \circ$.

The best fit (χ_{min}^2) was used to present the model along with the detected chords in Figure 2. We note that the posterior distribution for the pole orientation mirrors the adopted prior. Because the occultation chords alone do not independently constrain the rotational axis, the coordinates α_Q and δ_Q are treated throughout this work as fixed model inputs based on [Pereira et al. \(2023\)](#), rather than newly derived measurements.

The remaining fitted parameters correspond to the projected center of the ellipsoidal model on the tangent plane associated with each occultation event. Since the origin of each tangent plane is defined by the ephemeris position of Quaoar, the fitted center provides the offset relative to the ephemeris at the corresponding occultation epoch. This offset was further corrected for gravitational light deflection due to the Sun, Jupiter, and Saturn, treating the correction as a rigid translation of the fitted occultation geometry. The resulting offset was then applied to the ephemeris position of Quaoar, obtaining the astrometric positions, presented in Appendix C, Table 4

It was observed that, on certain dates, the data did not constrain the model, resulting in an individual χ^2 close to zero. In these cases, the MCMC algorithm sampled the center parameters (f_i, g_i) uniformly, indicating that the data were not sensitive to them. The conclusion is that their values are consistent with the prior range used in the simulation.

The ability of an individual event to constrain the global shape model depends on its chord coverage and the resulting balance in degrees of freedom. For each event, adjusting the center coordinates introduces two local free parameters (f_i, g_i), meaning that a successful constraint requires the observational geometric inputs to outweigh these added variables.

Multi-chord events with limited or asymmetric distribution may fail to restrict the model. Conversely, some few-chord events can provide significant constraints. For instance, the two-chord event of 2019-10-16, which consisted of a central chord and a northern chord, effectively restricted the global solution because its four limb points easily countered the two local center variables.

For single-chord events, providing a constraint is generally more challenging since the two extremity points match the two local degrees of freedom. However, central single chords can constrain the model if their measured lengths exceed the projected semi-minor axis b' , establishing a strict minimum size for the body. This is the case for the single-chord events of 2013-07-09, 2018-09-02, 2019-06-28, and 2019-08-04. On the other hand, single chords crossing far to the north or south of the body do not impose this size boundary; the center opti-

mization can freely shift them, driving their individual χ^2 close to zero without bounding the global parameters (e.g., the events of 2019-03-27, 2020-06-16, 2020-07-01, 2023-05-20, and 2023-05-24).

A unique case is the single-chord event of 2020-06-11. Although the positive chord is short, it is closely bounded by a negative chord. If Quaoar’s limb were larger than a specific threshold, it would intersect the negative chord’s path, invalidating the model. Therefore, the combination of this tight negative constraint makes the 2020-06-11 event highly effective in bounding the shape parameters.

Using only the events that constrain the model, we are left with a total of 23 occultations (2011-05-04, 2013-07-09, 2018-07-26, 2018-09-02, 2019-04-28, 2019-05-28, 2019-06-05, 2019-06-28, 2019-08-04, 2019-09-26, 2019-10-16, 2020-06-11, 2022-06-24, 2022-08-09, 2023-05-13, 2023-05-26, 2023-07-15, 2023-08-24, 2024-04-10, 2024-07-04, 2024-08-28, 2025-06-12, 2025-06-20), totalizing 90 chords, which means 180 points on Quaoar’s limb. Our minimum χ^2 , considering a sigma model of 2 km, was 179.6 for our MCMC fit. Therefore, the minimum χ^2 per degree of freedom for this fit was 0.998.

3.3. Atmosphere

We use the occultation light curves obtained during the August 9, 2022 occultation at Gemini North (z' band), which is our curve with the lowest dispersion and highest spatial resolution, to derive an upper limit for a global atmosphere around Quaoar. Using a direct ray tracing code, we generate synthetic light curves, following the protocol presented in [Dias-Oliveira et al. \(2015\)](#). We assume a CH_4 atmosphere and we use the same thermal profile $T(r)$ as [Braga-Ribas et al. \(2013\)](#), where r is the distance to Quaoar’s center. The $T(r)$ profile starts with a surface temperature of $T(r_{\text{surf}}) = 42$ K and a thermal gradient of $dT/dz(r_{\text{surf}}) = 5.7$ K km^{-1} , which ramps up to an isothermal branch at 102 K at an altitude of about $z = 10$ km, see [Morgado et al. \(2022\)](#). We fit synthetic light curves with various surface pressure p_{surf} to derive a $\chi^2(p_{\text{surf}})$ function.

We have applied this procedure to the three data sets obtained at Gemini (r' and z' bands) and at CFHT (Ks band). Concerning Gemini, the light curve obtained in the z' band has about twice the SNR obtained in the r' band. As a consequence, the latter does not bring significant improvement when compared to the z' band. On the other hand, the CFHT light curve has an SNR comparable to that of the Gemini z' band. However, diffraction effects limit the detection of an atmosphere in the immediate vicinity of the surface. Fresnel fringes are present over a typical distance of a few times $\lambda_F =$

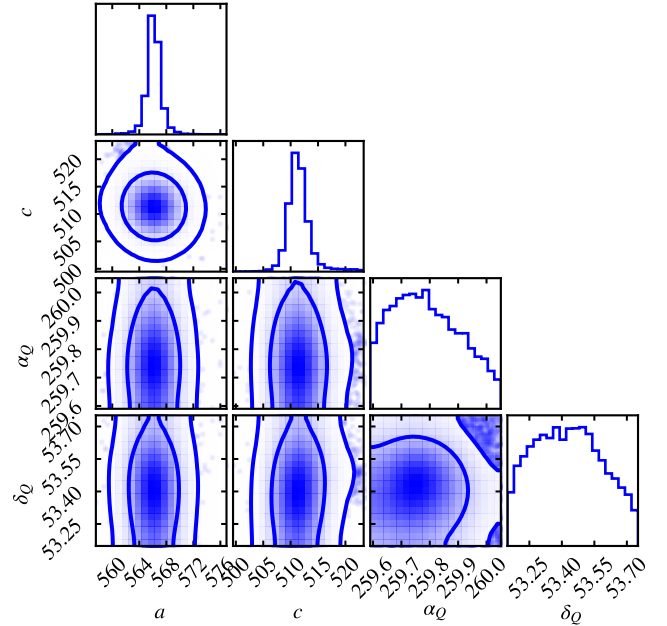


Figure 1. Corner plot showing the posterior probability distributions and correlations for the oblate ellipsoid model parameters. The samples used to generate this plot were obtained from an MCMC simulation and filtered to a χ^2 below $\chi^2_{\text{min}} + 100$. The histograms on the diagonal show the marginal probability distributions for each parameter. The off-diagonal plots show the joint probability distributions for each pair of parameters, revealing their correlations, and the level curves show the $1\text{-}\sigma$ and $3\text{-}\sigma$ regions. The fit is based on all the occultations.

$\sqrt{\lambda\Delta}/2$, where λ is the wavelength of observation, $\Delta = 42.0$ AU is the Quaoar geocentric distance in August 2022, and λ_F is the Fresnel scale. For the r' , z' and Ks bands (0.620, 0.947, 2.15 μm , respectively), we have $\lambda_F = 1.4, 1.7$ and 2.6 km, respectively.

Atmospheres with sub-nanobar surface pressure have detectable effects on the light curve below altitudes of ~ 10 km (Fig. 3). Thus, diffraction competes with atmospheric effects in this region. In principle, it is possible to disentangle the effects of diffraction and an atmosphere ([French & Gierasch 1976](#); [Sicardy & Dettwiller 2025](#)). In practice, however, we found that small changes in the modeling of the stellar disk luminosity profile or of possible local topographic features prevent the derivation of a Fresnel fringe pattern that is accurate enough to be disentangled from the small effects caused by a sub-nanobar atmosphere.

The CFHT light curve was obtained in the Ks band (2.15 μm), yielding the largest value of λ_F among the three light curves considered in this work. Consequently, most of the useful part of the CFHT light curve is dominated by diffraction effects and cannot be used for con-

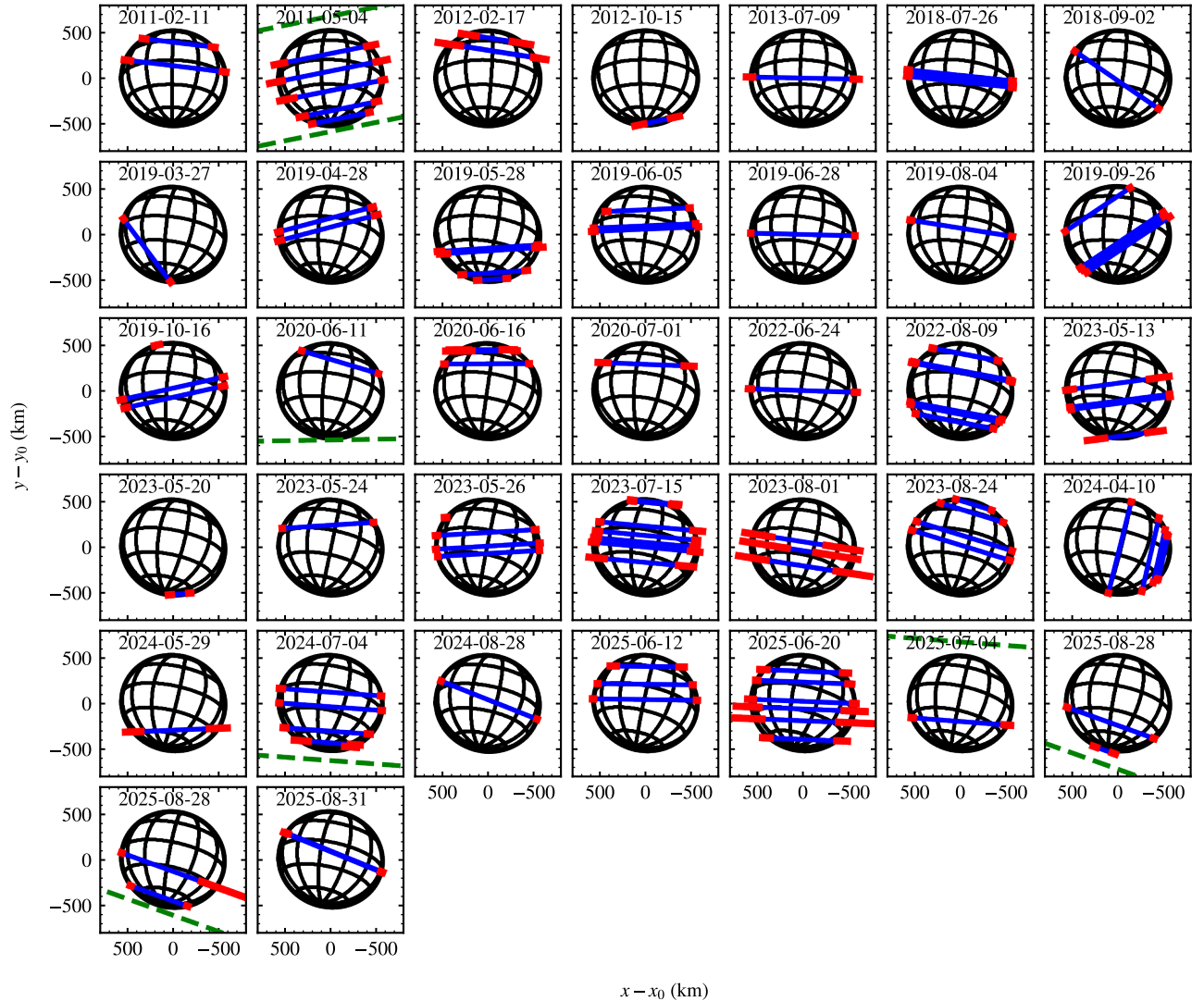


Figure 2. Best fit of the oblate ellipsoidal model: $a = b = 566.1$ km, $c = 511.2$ km, $\alpha_Q = 259.7^\circ$ and $\delta_Q = 53.4^\circ$. This model does not account for the rotation period or initial phase. The blue lines are the observed positive chords with their associated uncertainties, shown as red segments. The green dashed lines are the negative chords used to constrain the model. The 2025-08-28 occultation shows duplicated frames due to a dual detection of Quaoar, suggesting a possible duplicity in the target star. The fit where the star was too far from zero ephemeris was excluded from both the ellipsoid fitting and the determination of Quaoar’s astrometric position.

straining the presence of an atmosphere. Consequently, only the Gemini z' light curve is used in this work to derive an atmospheric upper limit.

The Fig. 3 presents our results. The immersion and emersion data points have been compared with models using various surface pressures. We found that the minimum value χ_{\min}^2 of χ^2 is obtained for $p_{\text{surf}} = 0$ nbar, meaning that no atmosphere is detected. Applying the $\chi_{\min}^2 + 1$ and $\chi_{\min}^2 + 9$ criteria, we obtain upper limits of $p_{\text{surf}} = 0.15$ nbar (1σ) and $p_{\text{surf}} = 0.65$ nbar (3σ). This result improves the 1σ upper limits obtained from other stellar occultations by Quaoar.

The same exercise assuming a CO atmosphere provides upper limits of $p_{\text{surf}} = 0.2$ nbar (1σ) and $p_{\text{surf}} = 0.85$ nbar (3σ). Assuming a N_2 , we obtain respective upper limits of $p_{\text{surf}} = 0.2$ nbar and $p_{\text{surf}} = 0.95$ nbar.

4. CONCLUSIONS

We present here a comprehensive analysis of 14 years of observations of stellar occultations by the large TNO (50000) Quaoar, obtained on 36 different occultation campaigns, which resulted in 107 chords. We implemented a method, using Markov Chain Monte Carlo (MCMC), to fit 76 parameters, assuming an oblate spheroid that shares its rotational pole with its rings,

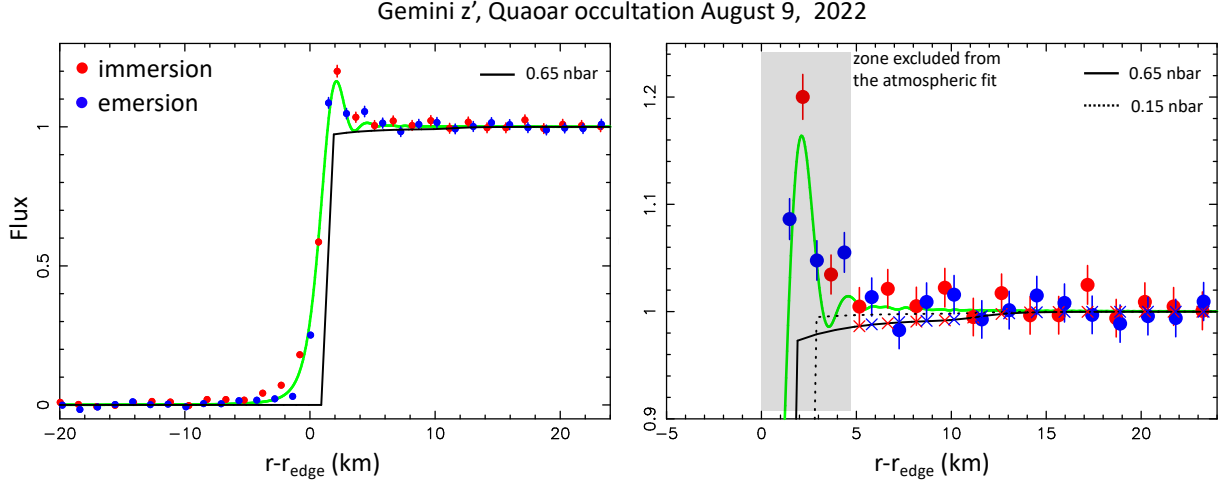


Figure 3. *Left panel:* the immersion (red) and emersion (blue) data points obtained at the the Gemini telescope (z' band) are plotted against their perpendicular distance to the local edge, $r - r_{\text{edge}}$, where r is the radial distance to Quaoar's center, known with a precision of 5.1 km, projected in the sky plane and r_{edge} is the fitted values of each edge radius. The green curve is the best-fitting Fresnel diffraction pattern accounting for the wavelength ($\lambda = 0.947 \mu\text{m}$), bandwidth ($\Delta\lambda = 0.236 \mu\text{m}$), stellar diameter (1.33 km), and finite integration time (1.5 km when projected in the sky plane). Although the diffraction model basically captures the presence of the main Fresnel fringe, some disagreement occurs, possibly due to unaccounted properties of the stellar disk profile or local topographic features. This means that in practice the data points within 5 km from the edge are not used in the fit. Also, the ray tracing program that generates the synthetic curves assumes purely geometric optics, i.e. ignores diffraction effects. The black curve is a synthetic light curve accounting for a CH_4 atmosphere with surface pressure $p_{\text{surf}} = 0.65 \text{ nbar}$, our 3σ upper limit for such atmosphere. *Right panel:* An enlarged version of the left panel, where the dotted line is a synthetic light curve for a CH_4 atmosphere with surface pressure $p_{\text{surf}} = 0.15 \text{ nbar}$, our 1σ upper limit for an atmosphere. The crosses indicate the points of the model that are used to calculate the χ^2 value of the fits.

and all parameters obtained for Quaoar using this model are summarized in Table 2.

Table 2. Summary results. The J2 and J4 were obtained using (Rossi et al. 1999) equations. All the values in this table are in $1\text{-}\sigma$ confidence level.

Variable	Result
Equatorial semi-axis ($a=b$)	$566.1_{-2.2}^{+2.5} \text{ km}$
Polar semi-axis (c)	$511.2_{-3.7}^{+3.6} \text{ km}$
Oblateness	0.097 ± 0.011
J2	0.03960 ± 0.00048
J4	-0.00222 ± 0.00005
D_e volumetric	$1,094.4 \pm 4.6 \text{ km}$
D_e area	$1,095.4 \pm 4.6 \text{ km}$
Density	$1.760 \pm 0.109 \text{ g/cm}^3$
Density Maclaurin	$1.859 \pm 0.200 \text{ g/cm}^3$
CH_4 upper limit p_{surf}	0.15 nbar
CO upper limit p_{surf}	0.20 nbar
N_2 upper limit p_{surf}	0.20 nbar

The oblate model we obtained has equatorial semi-axes of $566.1_{-2.2}^{+2.5} \text{ km}$, polar semi-axis of $511.2_{-3.7}^{+3.6} \text{ km}$, polar oblateness of 0.097 ± 0.011 that produces an equivalent surface diameter of $1,095.4 \pm 4.6 \text{ km}$ and an equiv-

alent volumetric diameter of $1,094.4 \pm 4.6 \text{ km}$. This can be compared to previous values reported by Braga-Ribas et al. (2013) of $1,110 \pm 5 \text{ km}$ in equivalent volumetric diameter and $0.090_{-0.018}^{+0.027}$ in oblateness. Using the obtained volume and the mass from Braga-Ribas et al. (2025), we derive a density of $1.760 \pm 0.109 \text{ g/cm}^3$. Alternatively, using the rotation period determined by Ortiz et al. (2003), the density calculated for a body in Maclaurin hydrostatic equilibrium with the here obtained dimensions is $1.859 \pm 0.200 \text{ g/cm}^3$. For more details on the Maclaurin density calculations, see Braga-Ribas et al. (2013), Ortiz et al. (2012), or Rommel et al. (2025). The density proposed by Braga-Ribas et al. (2013) was $1.99 \pm 0.46 \text{ g/cm}^3$, still consistent with the density found in our study, but based on old value for the system mass: $1.65 \pm 0.16 \times 10^{21} \text{ kg}$. Vachier et al. (2012).

We note that the density obtained from mass and volume and the one from the Maclaurin equilibrium figure overlap within uncertainties. This suggests that Quaoar may indeed be in hydrostatic equilibrium, thus strengthening the case for its classification as a dwarf planet.

Quaoar has an oblate shape and is in Maclaurin hydrostatic equilibrium implies a single-peaked rotation period of $8.8394 \pm 0.0002 \text{ hours}$. Consequently, the en-

tire amplitude of the rotational light curve must be attributed solely to albedo variegation. Furthermore, this model places the QR1 ring closer to the 1/6 spin-orbit resonance instead of the 1/3 and QR2 at 5/14 instead 5/7. These characteristics weaken the assumption that Quaoar is oblate and in hydrostatic equilibrium. This data set can also be used to explore a putative triaxial shape. Considering that the rotation light curve amplitude is caused by its shape or a combination of albedo variegation and shape, to account for the double peak solution and the 17.6788h rotation period.

A value for Quaoar’s absolute magnitude, $H_V = 2.79 \pm 0.35$, was derived by Kiss et al. (2024), eliminating the contributions from Weywot and the rings and using 2003 data originally published by Rabinowitz et al. (2007). To derive Quaoar’s geometric albedo, we used the model’s projected semi-axis $a' = 566.3 \pm 3.1$ km and $b' = 518.8 \pm 4.2$ km at the epoch of the absolute magnitude observation. With that, we obtain a geometric albedo of 0.125 ± 0.038 using the equation in Braga-Ribas et al. (2013). This result shows a small discrepancy when compared to the geometric albedo of 0.109 ± 0.007 proposed by Braga-Ribas et al. (2013), when no projection and higher absolute magnitude values were used.

Quaoar was one of the objects that potentially retained sufficient volatiles to sustain a global atmosphere Young et al. (2020). Therefore, the possible absence of a CH_4 atmosphere in Quaoar’s system, smaller than 0.15 nbar, aids in constraining the mechanisms responsible for maintaining volatiles in the outer solar system. We also duplicated our ray-tracing analysis for putative N_2 and CO atmospheres. The derived 1σ upper limits for these gases (both equal to 0.2) are higher than those for CH_4 . Considering these limits alongside the high volatility of these species, we conclude that the presence of global N_2 or CO atmospheres around Quaoar is highly improbable.

Finally, although the data set is fully explained by the oblate model presented here, we want to mention that other models, like a triaxial ellipsoid, may also be compatible. Therefore, Quaoar’s definitive tridimensional shape remains to be defined.

ACKNOWLEDGMENTS

This work is based on observations collected by a large network of institutions and individual observers whose collaboration and support were essential. We are grateful for the efforts in data acquisition, campaigns, and analysis. This work would not have been possible without the support of this community. We dedicate this work to Tony George, deceased. The

following observers have also contributed to data acquisition used in this work: A. Aia, M. Bachini, T. Bridges, P. Barroy, A. Barry, K. L. Bath, Z. Bora, G. Brabant, D. Briggs, S. Calavia, E. Campbell, G. Canaud, M. Conjat, M. Craciun, P. Delincak, I. Dinev, J. Dostal, S. Dostal, C. Drebber, E. Ducrot, B. Emptage, R. Evans, K. Hill, G. Holtkamp, R. Horvat, G. Hudson, E. Karampotsiou, P. Kilmartin, A. Klotz, M. Korec, P. Krabbendam, E. Lacruz, B. Lambert, B. Loader, J. Loucks, T. Mollier, E. Ogiza, J. Oliveira, A. Olsen, R. Paine, B. Paton, I. Pérez-García, J. Polák, J. Pollak, S. Pyrzas, C. Ratinaud, A. Ribera, S. Robinson, M. Rottenborn, L. Rousselot, M. Serrau, M. Serau, H. Simon, M. F. Skrutskie, P. Sogorb, J. Talbot, J. P. Tengk, S. Todd, D. Tomko, M. Unwin, D. Vernet, J. M. Vienney, W. Witte, and S. Yusuf. We gratefully acknowledge financial support from the following institutions and grants: This study was financed in part by the **Coordenação de Aperfeiçoamento de Pessoal de Nível Superior – Brasil (CAPES) – Finance Code 001**, and the **National Institute of Science and Technology of the e-Universe project (INCT do e-Universo)**, CNPq grant 465376/2014-2. FBR acknowledges **CNPq grant 316604/2023-2** and the financial support of the NAPI “Fenômenos Extremos do Universo” of **Fundação Araucária**. R. V-M thanks grant **CNPq 307368/2021-1**. MA acknowledges **CNPq 427700/2018-3**, **310683/2017-3**, and **473002/2013-2**, and **FAPERJ E-26/210.705/2024**. JIBC acknowledges **CNPq grants 305917/2019-6 and 306691/2022-1**, and **FAPERJ 201.681/2019**. T.F.L.L. Pinheiro acknowledges support from **CNPq - Proc.313994/2025-0**. CLP thanks the **FAPERJ/DSC-10 E-26/204.141/2022**, **FAPERJ/PDR-10 E-26/200.107/2025**, and **FAPERJ 200.108/2025**. GR acknowledges **FAPESP 2024/20150-1**. ARGJ thanks **FAPEMIG grant APQ-02987-24**. BEM thanks **CAPES Grant 23079.212658/2024-30**. BS acknowledges support by the French ANR project Roche, number ANR-23-CE49-0012. ER would like to thanks to Fundação de Amparo à Pesquisa do Estado do Rio de Janeiro (FAPERJ) for their support through a fellowship (E-26/204.602/2021). The authors are grateful to the IMPACTON team, in special to R. Souza, A. Santiago and A. Santos for the technical support in the observations at the Observatório Astronômico do Sertão de Itaparica (OASI). BEM thanks CAPES grant 23079.212658/2024-30, CNPq/Universal grant 408543/2025-6 and FAPERJ grant E-26/204.205/2025.. Support was also provided by the **Fundação de Amparo à Pesquisa e Inovação do Espírito Santo (FAPES)**, No.

2021-X4ZNX. Further support from **CNPq** (project 307400/2025-5), the **State Secretariat of Science, Technology, and Higher Education of Paraná (SETI-Fundo Paraná, grant 031/2024)** is acknowledged. We acknowledge funding from the **European Research Council (ERC)** under the European Community’s H2020 (2014-2020/ERC Grant Agreement no. 669416, “LUCKY STAR”), the **ERC AdG SUBSTELLAR** (GA 101054354), and ERC grant agreement n° 803193/BEBOP. **HiPERCAM** was funded by the **European Research Council under the European Union’s Seventh Framework Programme (FP/2007-2013)** under **ERC-2013-ADG Grant Agreement no. 340040 (HiPERCAM)**, with additional funding for operations and enhancements provided by the **UK Science and Technology Facilities Council (STFC)**. J.L.O., Y.K., P.S.-S., N.M., M.V.-L., J.M.G.L and R.D. acknowledge financial support from the Severo Ochoa grant **CEX2021-001131-S** (MCIN/AEI/10.13039/501100011033) and Spanish projects **PID2020-112789GB-I00** (AEI) and **Proyecto de Excelencia de la Junta de Andalucía PY20-01309**. P.S.-S. and Y.K. acknowledge financial support from the Spanish I+D+i project **PID2022-139555NB-I00**. T.S.-R. acknowledges funding from **PID2021-125883NB-C21**. Further Spanish support includes grants **PID2021-122842OB-C21** and **CEX2019-000918-M**. J. M. Gómez-Limón acknowledges funding from the university training programme **FPU2022/00492**. Operation of the **University of Haifa’s H80 (800.0) telescope at the Wise Observatory** is partly supported by ISF grant 3200/20. Observations were also collected at the Wise Observatory with the C28 (711.0) Jay Baum Rich telescope. This article includes observations made in the **Two-meter Twin Telescope (TTT)** at the Teide Observatory of the **IAC**, operated by Light Bridges, and supported by Indefeasible Computer Rights (ICR) through PEI “PLANETIX25.” The photometric observations from the **University of Athens Observatory (UOAO)** utilized robotic instruments (Gazeas 2016). The authors acknowledge the use of Sonja Itting-Enke’s C14 telescope and the facilities at the Cuno Hoffmeister Memorial Observatory (CHMO). **IST40**, one of the observational facilities of the Istanbul University Observatory, was funded by the Scientific Research Projects Coordination Unit of Istanbul University (BAP-3685 and FBG-2017-23943). We also wish to thank the **Adiyaman University Astrophysics Application and Research Center (Türkiye)** for their support and collaboration. The **Joan Oró Telescope (TJO)** at the Montsec Observatory (OdM) is acknowledged,

as are observations made with the **Tx40 telescope at the Observatorio Astrofísico de Javalambre (OAJ)**. Partially based on observations collected at the **La Silla European Southern Observatory**. The 1.2-m Kryoneri telescope is operated by the Institute for Astronomy, Astrophysics, Space Applications and Remote Sensing of the National Observatory of Athens. Individual acknowledgments include: Funding for KB was provided by the European Union **ERC AdG SUBSTELLAR, GA 101054354**, E. S. thanks the **Adiyaman University Astrophysics Application and Research Center** for their support in the acquisition of data with the **ADYU60 telescope**. Work of KH supported by the project **RVO:67985815**. R.S. acknowledges funding from the **K-138962 grant** (NKFIH, Hungary). A. Takey and E.G. Elhosseiny acknowledge financial support from the **Egyptian Science, Technology & Innovation Funding Authority (STDF)** under grant number 48102. A. Liakos acknowledges financial support by the **European Space Agency** under the NELIOTA program. The contributions of R. Scott Fisher were funded by the **Heising-Simons Foundation through grant 2023-4845**. D.I. acknowledges funding by the **University of Belgrade - Faculty of Mathematics** through grant from the **Ministry of Science, Technological Development and Innovation of the Republic of Serbia** (contract No. **451-03-136/2025-03/200104**). O.V. acknowledges support by the **Astronomical station Vidojevica**, funding from the **Ministry of Science, Technological Development and Innovation of the Republic of Serbia** (contract No. **451-03-136/2025-03/200002**), by the **EC** through project **BELISSIMA** (call **FP7-REGPOT-2010-5**, No. **265772**), and **Chinese Academy of Sciences (CAS) President’s International Fellowship Initiative (PIFI)** (grant No. **2024VMB0006**). Q.C.T. and S.R. wish to thank **Roy Kilgard** for his assistance at the 24-inch telescope at Van Vleck Observatory. We thank the **Friends of MIRA** for their support. This publication uses data products from the observational networks and research programs. This publication uses data products from the **ESO La Silla Observatory**. We gratefully acknowledge support from the **SPECULOOS** network and the **TRAPPIST** project (Jehin et al. 2011). The **TRAPPIST** project is funded by the **Belgian F.R.S.-FNRS** under grant **PDR T.0120.21**. **E.J.** and **M.G.** are directors of research at the **FNRS**. The ULiege’s contribution to SPECULOOS has received funding from the **European Research Council (ERC)** under the European Union’s Seventh Framework Programme (FP/2007-2013) (grant Agreement n°

336480/SPECULOOS), from the **Balzan Prize and Francqui Foundations**, from the **Belgian Scientific Research Foundation (F.R.S.-FNRS; grant n° T.0109.20)**, from the University of Liege, and from the **ARC grant** financed by the Wallonia-Brussels Federation. J.d.W. and MIT gratefully acknowledge financial support from the **Heising-Simons Foundation**, Dr. and Mrs. Colin Masson and Dr. Peter A. Gilman for **Artemis** (the first telescope of the SPECULOOS-North Observatory situated in Tenerife, Spain). M.G. is F.R.S-FNRS Research Director. E.J. and M.G. are Directors of Research at the Belgian F.R.S.-FNRS.

SPECULOOS and related projects are further supported by the **Swiss National Science Foundation** (PP00P2-163967, PP00P2-190080 and the **National Centre for Competence in Research PlanetS**). Support was also received from the **Simons Foundation (PI Queloz, grant number 327127)**, and the **European Research Council (ERC)** under the European Union’s Horizon 2020 research and innovation programme (grant agreement n° 803193/BEBOP), from the **MERAC foundation**, and from the **Science and Technology Facilities Council (STFC; grant n° ST/S00193X/1)**.

APPENDIX

A. STAR INFORMATION

This appendix provides detailed astrometric and photometric information for the stellar sources used in the analysis of the Quaoar occultations. Table 3 lists the parameters for each candidate star involved in a successful occultation event. These parameters include the star’s coordinates and magnitude from the Gaia DR3 catalog, the estimated stellar angular diameter, and the predicted event velocity relevant to the occultation geometry.

Table 3. Stellar occultation candidates. The columns are: Event (date of the occultation), Designation (GaiaDR3 Source ID), R.A. (ICRS star Right Ascension at epoch), Decl. (ICRS star Declination at epoch), G (star’s magnitude in the Gaia G-band), star angular diameter for a main sequence star calculated using [Van Belle \(1999\)](#) equations and predicted event velocity.

Event	Designation	R.A. h m s ± mas	Decl. d m s ± mas	G mag	star d. mas	ev. vel. km/s
2011-02-11	4136779291133721856	17 28 47.6205987 +/- 0.133	-15 41 59.088361 +/- 0.182	15.6	0.038	20.3
2011-05-04	4136810730296078208	17 28 50.8012677 +/- 0.149	-15 27 42.725259 +/- 0.191	15.6	0.019	-18.3
2012-02-17	4125098801168495104	17 34 21.8456254 +/- 0.088	-15 42 10.493594 +/- 0.110	14.8	0.039	18.5
2012-10-15	4136784376375275264	17 28 10.1277047 +/- 0.187	-15 36 23.267173 +/- 0.261	16.9	0.008	20.0
2013-07-09	4125147729438520576	17 34 40.4637157 +/- 0.051	-15 23 37.568216 +/- 0.062	14.4	0.025	-22.5
2018-07-26	4145438426258652032	18 00 39.4071069 +/- 0.099	-15 21 58.417719 +/- 0.112	16.0	0.023	-20.0
2018-09-02	4145444851530756224	17 59 02.0588533 +/- 1.224	-15 27 30.206675 +/- 1.228	12.7	0.122	-6.3
2019-03-27	4145808549349443456	18 12 50.7872483 +/- 0.700	-15 27 52.149623 +/- 0.629	19.0	0.020	5.5
2019-04-28	4145998451292755840	18 12 23.2150735 +/- 0.956	-15 22 07.193200 +/- 0.957	18.7	0.010	-12.3
2019-05-28	4146010893851176704	18 10 38.9330116 +/- 0.233	-15 18 37.726232 +/- 0.296	16.8	0.023	-21.9
2019-06-05	4146058516454329344	18 10 07.3111037 +/- 0.356	-15 18 12.353542 +/- 0.438	17.4	0.035	-23.2
2019-06-28	4145978492632029696	18 08 15.5287147 +/- 0.116	-15 17 58.148575 +/- 0.135	15.7	0.106	-24.6
2019-08-04	4146716230551709696	18 05 34.7866006 +/- 0.130	-15 21 02.046296 +/- 0.143	15.8	0.026	-17.8
2019-09-26	4145210002691776000	18 04 27.3879636 +/- 0.128	-15 30 01.808631 +/- 0.152	15.5	0.010	7.3
2019-10-16	4146695060624747264	18 05 07.9990422 +/- 0.153	-15 33 24.821037 +/- 0.177	16.2	0.010	16.1
2020-06-11	4146202445050212352	18 15 03.0557899 +/- 0.064	-15 15 04.946217 +/- 0.064	12.7	0.034	-24.0
2020-06-16	4145839022104776192	18 14 40.8010099 +/- 0.210	-15 15 02.309810 +/- 0.276	16.1	0.011	-24.4
2020-07-01	4145841908322772736	18 13 25.4865633 +/- 0.392	-15 15 23.885899 +/- 0.474	17.4	0.010	-24.5
2022-06-24	4098181274706042624	18 25 04.0901845 +/- 0.464	-15 07 59.491317 +/- 0.539	16.9	0.020	-24.7
2022-08-09	4098214367441486592	18 21 42.8696462 +/- 0.240	-15 12 45.963919 +/- 0.219	15.3	0.094	-17.6
2023-05-13	4103283867659271424	18 33 31.7127652 +/- 0.271	-15 04 52.193652 +/- 0.261	15.2	0.012	-15.8
2023-05-20	4103284421808448768	18 33 09.7151861 +/- 0.397	-15 04 16.183796 +/- 0.435	16.5	0.022	-18.1

Table 3 – Continuation

Event	Designation	R.A. h m s \pm mas	Decl. d m s \pm mas	G mag	star d. mas	ev. vel. km/s
2023-05-24	4103286105383315840	18 32 52.8648095 \pm 0.246	-15 03 56.396132 \pm 0.317	15.3	0.036	-19.4
2023-05-26	4103286891316477056	18 32 44.9288941 \pm 0.195	-15 03 48.978547 \pm 0.199	14.8	0.038	-20.0
2023-07-15	4103961617817078400	18 28 56.6548653 \pm 0.832	-15 05 12.815200 \pm 1.063	17.8	0.010	-23.7
2023-08-01	4103986872241883008	18 27 39.0746912 \pm 1.737	-15 07 33.231370 \pm 1.599	18.7	0.010	-20.2
2023-08-24	4103983505031369088	18 26 27.7596490 \pm 1.123	-15 11 20.147339 \pm 0.354	16.9	0.014	-12.9
2024-04-10	4103400420265295488	18 39 51.9082536 \pm 0.142	-15 04 33.742587 \pm 0.179	13.8	0.026	-4.1
2024-05-29	4103441029097671680	18 37 58.1148584 \pm 2.364	-14 58 37.782025 \pm 1.577	18.5	0.010	-20.6
2024-07-04	4103264802318239360	18 35 10.7002403 \pm 0.694	-14 59 34.936931 \pm 0.726	17.2	0.008	-24.6
2024-08-28	4103291293710742656	18 31 41.2280262 \pm 1.171	-15 07 52.300912 \pm 1.222	18.0	0.010	-11.8
2025-06-12	4103487277307240704	18 42 29.3682255 \pm 0.407	-14 53 02.547910 \pm 0.561	16.1	0.033	-23.1
2025-06-20	4103489407614726016	18 41 49.2834017 \pm 1.502	-14 53 18.937250 \pm 1.322	18.2	0.011	-24.2
2025-07-04	4103410659417963520	18 40 41.6345537 \pm 0.745	-14 54 18.517783 \pm 0.832	13.3	0.492	-24.7
2025-08-28	4103437150790068352	18 37 10.4131641 \pm 0.998	-15 02 54.481853 \pm 1.293	16.3	0.010	-12.2
2025-08-31	4103436390532307456	18 37 03.1467727 \pm 0.703	-15 03 35.634275 \pm 0.738	17.1	0.008	-10.9

B. LIGHT CURVES

This appendix presents the set of positive light curves obtained from all stellar occultation events utilized in this work. Light curves that have been previously published are not included in this work. Figures 4, 5, and 6 display the normalized flux as a function of time, ordered chronologically. Each light curve includes the normalized flux ratio (black points), the background flux from the star-free region (blue points), the theoretical geometric light curve (solid yellow line), and the final fitted model (solid red line).

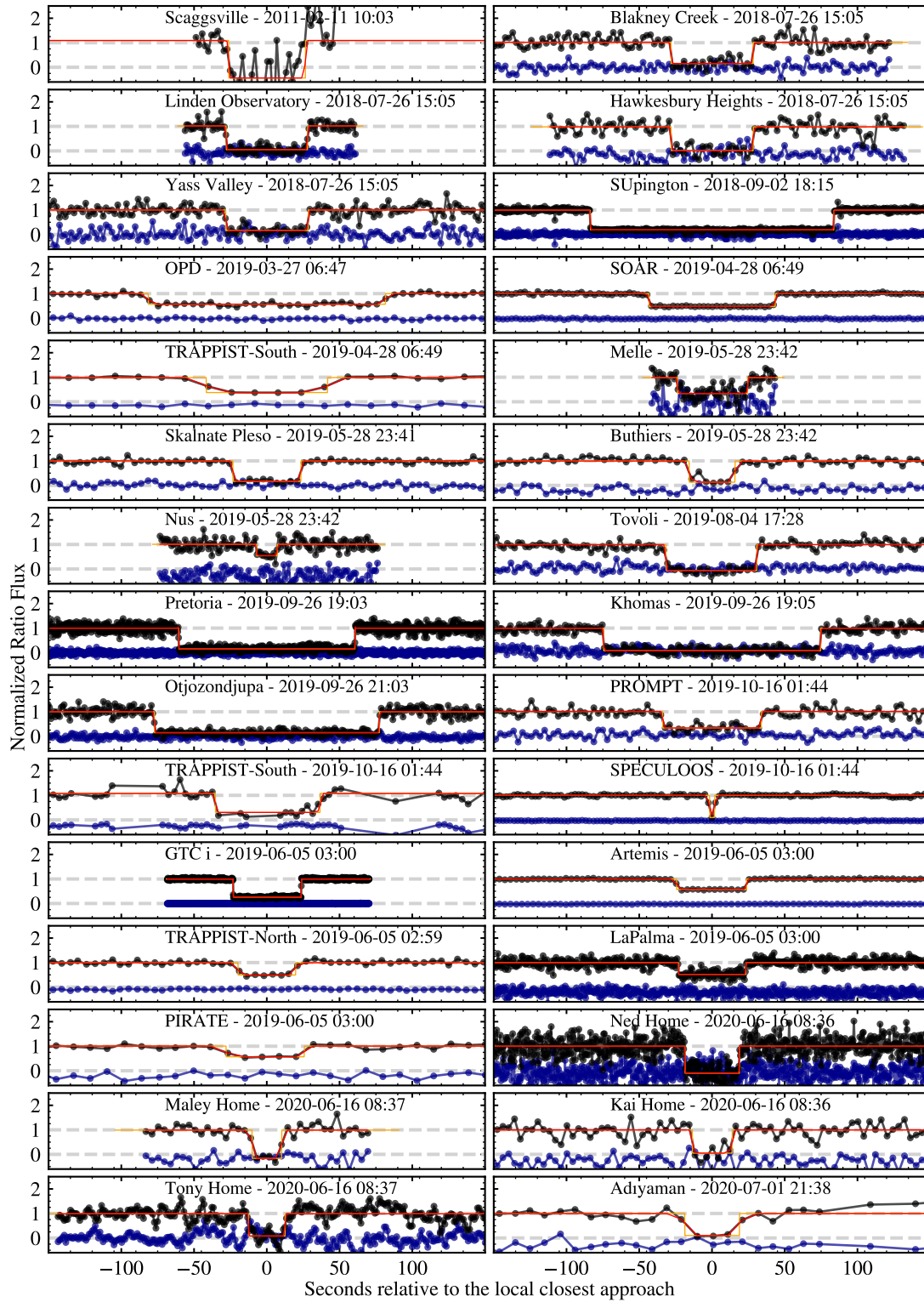


Figure 4. Light curves of Quaoar’s occultations that occurred between 2011 and 2020. Black line points represent the normalized target/calibrator flux ratio, while blue line points represent the flux from a star-free region of the sky near the target (ghost). The solid yellow line is the geometric light curve, and the solid red line is the light curve model.

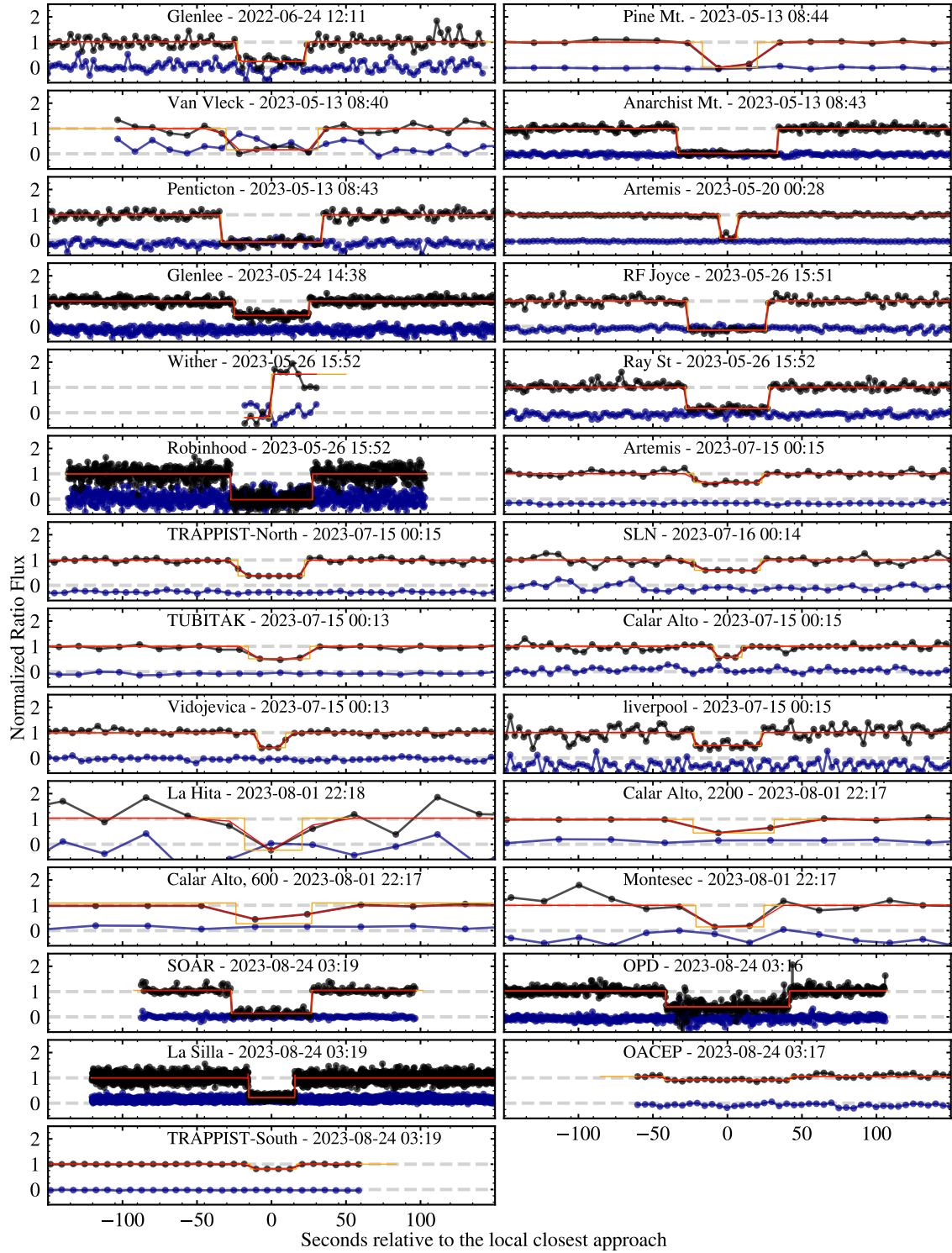


Figure 5. Light curves of Quaoar’s occultations that occurred between 2022 and 2023. Black line points represent the normalized target/calibrator flux ratio, while blue line points represent the flux from a star-free region of the sky near the target (ghost). The solid yellow line is the geometric light curve, and the solid red line is the light curve model.

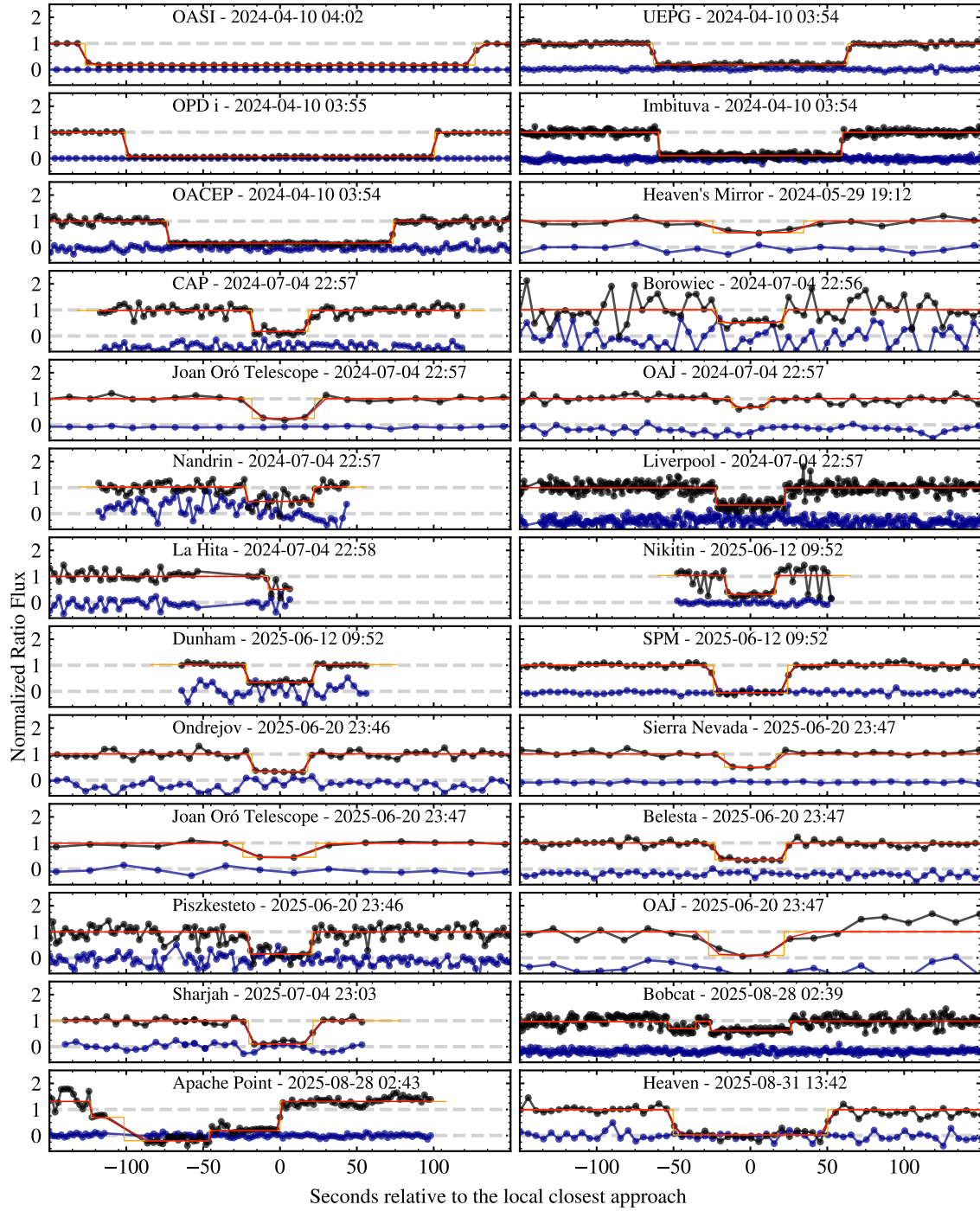


Figure 6. Light curves of Quaoar’s occultations that occurred between 2024 and 2025. Black line points represent the normalized target/calibrator flux ratio, while blue line points represent the flux from a star-free region of the sky near the target (ghost). The solid yellow line is the geometric light curve, and the solid red line is the light curve model.

C. NEW ASTROMETRIC POSITION

This appendix presents the astrometric positions of Quaoar derived from the stellar occultations analysed in this work. For each event, the fitted center of the ellipsoidal model provides the offset of Quaoar relative to its ephemeris position (NIMAv19) on the corresponding tangent plane. The occultation geometry was constructed using the Gaia DR3 astrometric position of the occulted star.

The fitted offsets were corrected for gravitational light deflection due to the Sun, Jupiter, and Saturn using the post-Newtonian formulation of [Klioner \(2003\)](#). For each deflecting body, we computed the differential deflection between the stellar ray and the finite-distance direction associated with the ephemeris position of Quaoar. The individual contributions were combined vectorially and applied as a rigid translation of the fitted occultation geometry on the tangent plane, following the occultation-specific formulation of [Poiani et al. \(2026\)](#).

The corrected offsets were then applied to the ephemeris position of Quaoar to obtain the final astrometric coordinates at the time of closest approach for each occultation event. These positions are listed in Table 4.

Table 4. This table contains Quaoar’s astrometric positions at the time of closest approach for each stellar occultation. These positions have been corrected for the gravitational deflection caused by the Sun, Jupiter and Saturn.

Event	f (km)	g (km)	df (km)	dg (km)	R.A. h m s ± mas	Decl. d m s ± mas
2011-02-11 10:05:49.940	-10.2 ± 68.8	-18.0 ± 82.0	-5.0	0.7	17 28 47.6192086 ± 3.164	-15 41 58.929638 ± 3.025
2011-05-04 02:38:30.680	-4.3 ± 10.4	22.0 ± 24.7	-1.0	-0.1	17 28 50.7999863 ± 0.369	-15 27 42.812496 ± 0.827
2012-02-17 04:30:44.960	37.4 ± 62.6	11.7 ± 88.3	-4.6	0.5	17 34 21.8438798 ± 1.985	-15 42 10.328825 ± 2.798
2012-10-15 00:41:18.820	0.0 ± 100.0	0.0 ± 100.0	5.0	0.1	17 28 10.1273220 ± 3.171	-15 36 23.292881 ± 3.176
2013-07-09 02:40:03.760	0.0 ± 100.0	0.0 ± 100.0	0.6	-0.2	17 34 40.4636051 ± 3.274	-15 23 37.482333 ± 3.274
2018-07-26 15:08:21.300	25.0 ± 15.7	-3.6 ± 90.2	0.9	-0.2	18 00 39.4079045 ± 0.524	-15 21 58.514347 ± 2.959
2018-09-02 18:16:51.600	-478.2 ± 33.2	-508.4 ± 44.0	2.1	-0.1	17 59 02.0596130 ± 1.630	-15 27 30.258388 ± 1.881
2019-03-27 06:56:33.480	-6.3 ± 24.2	58.8 ± 22.9	-2.8	-0.1	18 12 50.7835708 ± 1.049	-15 27 52.104642 ± 0.969
2019-04-28 06:47:02.040	44.9 ± 55.1	0.0 ± 100.0	-1.5	-0.2	18 12 23.2137245 ± 2.034	-15 22 07.269225 ± 3.398
2019-05-28 23:40:49.480	-40.7 ± 40.0	-5.0 ± 32.2	-0.6	-0.2	18 10 38.9338179 ± 1.335	-15 18 37.534872 ± 1.099
2019-06-05 03:00:57.040	-21.6 ± 4.6	59.9 ± 25.8	-0.5	-0.2	18 10 07.3114764 ± 0.386	-15 18 12.210859 ± 0.954
2019-06-28 12:35:40.720	-3.0 ± 4.4	-8.9 ± 62.1	0.1	-0.2	18 08 15.5284488 ± 0.186	-15 17 57.989302 ± 2.052
2019-08-04 17:24:51.320	5.7 ± 32.1	0.0 ± 100.0	1.1	-0.2	18 05 34.7868586 ± 1.061	-15 21 02.068371 ± 3.280
2019-09-26 18:55:33.920	-6.3 ± 4.0	32.1 ± 4.7	3.0	0.1	18 04 27.3892080 ± 0.181	-15 30 01.779453 ± 0.214
2019-10-16 01:39:00.780	15.9 ± 37.5	25.8 ± 13.9	4.2	0.2	18 05 07.9984539 ± 1.206	-15 33 24.860443 ± 0.478
2020-06-11 16:32:13.560	13.4 ± 6.2	14.5 ± 9.1	-0.3	-0.2	18 15 03.0558375 ± 0.215	-15 15 04.934584 ± 0.306
2020-06-16 08:38:20.160	-33.2 ± 22.4	9.0 ± 30.5	-0.2	-0.2	18 14 40.8009527 ± 0.766	-15 15 02.166913 ± 1.042
2020-07-01 21:38:55.520	0.0 ± 100.0	0.0 ± 100.0	0.2	-0.2	18 13 25.4861259 ± 3.320	-15 15 23.732643 ± 3.331
2022-06-24 12:09:29.520	24.8 ± 55.6	0.0 ± 100.0	-0.1	-0.2	18 25 04.0903196 ± 1.894	-15 07 59.527209 ± 3.347
2022-08-09 06:34:02.600	-21.0 ± 2.6	-5.1 ± 4.4	1.1	-0.1	18 21 42.8677879 ± 0.255	-15 12 45.829889 ± 0.263
2023-05-13 08:40:33.160	39.7 ± 8.3	37.3 ± 28.7	-1.2	-0.2	18 33 31.7144466 ± 0.385	-15 04 52.022706 ± 0.979
2023-05-20 00:24:21.460	0.0 ± 100.0	-3.6 ± 63.7	-1.0	-0.2	18 33 09.7160077 ± 3.311	-15 04 16.055219 ± 2.139
2023-05-24 14:36:05.100	17.1 ± 10.2	18.3 ± 20.5	-0.9	-0.2	18 32 52.8646139 ± 0.417	-15 03 56.444422 ± 0.746
2023-05-26 15:53:07.440	34.4 ± 6.0	3.1 ± 35.2	-0.9	-0.2	18 32 44.9285463 ± 0.277	-15 03 49.081984 ± 1.176
2023-07-15 00:16:17.840	81.7 ± 18.3	-31.2 ± 35.9	0.4	-0.2	18 28 56.6541066 ± 1.029	-15 05 12.672837 ± 1.592
2023-08-01 22:18:44.900	0.0 ± 100.0	0.0 ± 100.0	0.8	-0.1	18 27 39.0728406 ± 3.724	-15 07 33.063778 ± 3.662
2023-08-24 03:22:10.460	12.0 ± 4.6	-12.8 ± 6.0	1.5	-0.1	18 26 27.7618401 ± 1.134	-15 11 20.245411 ± 0.405
2024-04-10 03:58:50.740	-52.2 ± 5.0	58.4 ± 3.2	-2.4	-0.2	18 39 51.8964551 ± 0.215	-15 04 33.772079 ± 0.206
2024-05-29 19:15:55.320	0.0 ± 100.0	0.0 ± 100.0	-0.8	-0.2	18 37 58.1146688 ± 4.057	-14 58 37.852399 ± 3.655
2024-07-04 22:57:30.880	1.5 ± 14.3	-8.9 ± 69.8	0.1	-0.2	18 35 10.6992779 ± 0.839	-14 59 34.749734 ± 2.420
2024-08-28 10:38:30.040	62.4 ± 32.5	-29.9 ± 70.1	1.6	-0.1	18 31 41.2281212 ± 1.582	-15 07 52.300062 ± 2.600
2025-06-12 09:53:32.740	-6.3 ± 13.4	-12.0 ± 41.8	-0.5	-0.2	18 42 29.3680578 ± 0.601	-14 53 02.399948 ± 1.491

Table 4 – Continuation

Event	f (km)	g (km)	df (km)	dg (km)	R.A. h m s ± mas	Decl. d m s ± mas
2025-06-20 23:46:41.500	85.7 ± 14.3	52.5 ± 47.5	-0.3	-0.2	18 41 49.2831008 ± 1.575	-14 53 18.759540 ± 2.054
2025-07-04 23:06:15.360	-63.4 ± 36.6	0.0 ± 100.0	0.1	-0.2	18 40 41.6337573 ± 1.423	-14 54 18.400168 ± 3.414
2025-08-28 02:44:10.100	-55.9 ± 38.9	-35.3 ± 30.2	1.5	-0.05	18 37 10.4092945 ± 1.618	-15 02 54.335238 ± 1.629
2025-08-31 13:46:22.600	75.2 ± 24.8	40.9 ± 59.1	1.7	-0.03	18 37 03.1506750 ± 1.074	-15 03 35.760080 ± 2.070

D. OBSERVATIONAL INFORMATION

This appendix provides a summary of the observational campaigns, including successful occultation detections, as well as negative and unsuccessful observations. Due to the multi-site nature of this work, the following tables serve to document the instrumentation and the geographical location of each observer. To accommodate the extensive dataset, the observation logs have been combined and divided into two continuous tables linked by a unique observation ID. Table 5 details the setup and status of each event (e.g., Positive, Negative, 'Overcast', or 'Technical failure'), along with the observing site, telescope aperture, and camera model. Table 6 provides the corresponding timing and coordinate parameters, including exposure and cycle times, ingress and egress times, and the resulting chord lengths. We note that previously published positive events are not included here unless new timing information was derived, and observation campaigns consisting exclusively of non-detection chords are not presented in this work.

Table 5. Observational data for all Quaoar events: Part 1 (Setup and Status).

id	Date	Site	Country	Observer	Ap. (mm)	Camera	Time	Status
001	2011-02-11		U.S.A.	A. Scheck	203.0	MallinCam	GPS	Positive
002	2018-07-26		Australia	W. Hanna	508.0	QHY174M	GPS	Positive
003	2018-07-26		Australia	D. Herald	40.0	Watec 910BD	GPS	Positive
004	2018-07-26		Australia	D. Gault	30.0	Watec 910BD	GPS	Positive
005	2018-07-26		Australia	T. Barry	750.0	Point Grey 2855M	NTP	Positive
006	2018-09-02		South Africa	M. Kretlow		Raptor 247	GPS	Positive
007	2019-03-27	OPD	Brasil	F. L. Rommel	1600.0	IXon 4269	GPS	Positive
008	2019-04-28	SOAR	Chile	J. I. B. Camargo	4100	Raptor 247	GPS	Positive
009	2019-04-28	TRAPPIST-South	Chile	E. Jehin	600	FLI ProLine	GPS	Positive
010	2019-05-28	Ciprian		C. Vintdevará				Subsampled Star
011	2019-05-28	Saint-Caprais/Rabastens		E. Frappa	940	Watec 910HX	GPS	Overcast
012	2019-05-28	Nick Haigh - UK		N. J. Haigh	300	assi1600		Overcast
013	2019-05-28	Pallini		V. Tsamis	400	ATIK 16 HR		Technical failure
014	2019-05-28	C2PU		J.P. Rivet	1040	iXon Ultra 888	GPS	Overcast
015	2019-05-28	Adiyaman Observatory		E. Sonbas	600	Andor Ikon-m 934	GPS	Negative
016	2019-05-28	Kryoneri		A. Liakos	1200	Apogee Aspen CG47	GPS	Negative
017	2019-05-28	Puimichel		J. Lecacheux	105	Raptor 247	GPS	Negative
018	2019-05-28	Vlad Dumitrescu		V. Dumitrescu		ZWO ASI1600		Subsampled Star
019	2019-05-28	UOAO		K. Gazeas	400	SBIG STF-3200W		Negative
020	2019-05-28		Italy	V. Aosta		Raptor ???	GPS	Positive
021	2019-05-28	Skalnate Pleso	Slovakia	R. Komzik	1300	FLI ProLine	NTP	Positive
022	2019-05-28		Germany	O. Eberhard	0.6 m	Watec 910 HX	GPS	Positive
023	2019-05-28		France	A. Leroy	600	QHY174M	GPS	Positive
024	2019-06-05	GTC	Spain	J. L. Ortiz	10.4 m	HiPERCAM	GPS	Positive
025	2019-06-05	Sanchez		C. Sánchez				Technical failure
026	2019-06-05	TRAPPIST-North	Morocco	E. Jehin	0.6 m	Andor IKONL	GPS	Positive
027	2019-06-05	PIRATE Mark III	Spain	U. Kolb	0.425 m	FLI PL 16803	GPS	Positive
028	2019-06-05	Liverpool	Spain	P. S. Sanz	2.0 m	RISE	GPS	Positive
029	2019-06-05	Artemis	Spain	E. Jehin	1.0 m	Andor iKon-L	GPS	Positive
030	2019-08-04	Tovoli	Namibia	K. Poschinger	350	ZWO ASI 174 MM	GPS	Positive
031	2019-09-26	Wolfgang Hakos		W. Beisker				Technical failure
032	2019-09-26	Les Makes		J. P. Teng				Overcast
033	2019-09-26		South Africa	C. Foster	0.355	ZWO ASI290MM	NTP	Positive
034	2019-09-26		Namibia	W. Beisker	0.35 m	Raptor 247	GPS	Positive
035	2019-09-26		Namibia	M. Backes	0.35 m	Raptor 247	GPS	Positive
036	2019-09-26		Namibia	M. Kretlow		Raptor 247	GPS	Positive
037	2019-10-16	SPECULOOS	Chile	E. Jehin	1000	Andor IKONL	GPS	Positive
038	2019-10-16	PROMPT5	Chile	J. Pollock	400	AltaU-47	NTP	Positive

Table 5 continued

Table 5 (continued)

id	Date	Site	Country	Observer	Ap. (mm)	Camera	Time	Status
039	2019-10-16	TRAPPIST-South	Chile	E. Jehin	600	FLI ProLine	GPS	Positive
040	2020-06-16		U.S.A	T. George	300	WAT-910HX	GPS	Positive
041	2020-06-16		U.S.A	P. Maley		WAT-910HX	GPS	Positive
042	2020-06-16		U.S.A	K. Getrost	254	QHY174M	GPS	Positive
043	2020-06-16		U.S.A	N. Smith		QHY174M	GPS	Positive
044	2020-07-01	AUO	Turkey	W. Ogloza	600	Andor Tech	GPS	Positive
045	2022-06-24		Australia	S. Kerr	304	Watec 910BD	GPS	Positive
046	2023-05-13	MIRA		K. Bender	914	Watec 910hx/rc	GPS	Negative
047	2023-05-13	Olsen Urbana - Illinois		A. Olsen	508	QHY174M	GPS	Overcast
048	2023-05-13	Harvest Moon		S. Messner	450	WAT-910HX-RC	GPS	Overcast
049	2023-05-13	Naylor		R. Kamin	355	QHY174M	GPS	Overcast
050	2023-05-13	Swift Home		T. Swift	200	Watec910HX/RC	GPS	Technical failure
051	2023-05-13	HAA-Occultation-Mobil		J. J. Kavelaars	305	QHY174M	GPS	Technical failure
052	2023-05-13	Mendel Observatory		C. Duston	457	Moravian-C4	GPS	Technical failure
053	2023-05-13	MIRA		R. Nollthenius	356	Watec 910hx/rc	GPS	Negative
054	2023-05-13		U.S.A	Q. C. Tian	610	FLI PL4240	PC Time	Positive
055	2023-05-13		U.S.A	S. Fisher	356	Andor F9000	PC Time	Positive
056	2023-05-13		Canada	B. Gowe	400	QHY174M	GPS	Positive
057	2023-05-13		Canada	P. Ceravolo	355	QHY174M	GPS	Positive
058	2023-05-20	Artemis	Spain	A. Burdanov	1000	Andor iKon-L	GPS	Positive
059	2023-05-24	Mt John		A. Gilmore	610	Watec 120N+	GPS	Negative
060	2023-05-24	Murrumbateman		D. Herald	400	Watec 910BD	GPS	Negative
061	2023-05-24	Linden		T. Barry	750	Point Grey 28S5M	GPS	Negative
062	2023-05-24	Heaven's Mirror		W. Hanna	508	QHY174M	GPS	Negative
063	2023-05-24		Australia	S. Kerr	304	Watec 910BD	GPS	Positive
064	2023-05-26		New Zealand	A. Pennell	350	Watec 910BD	GPS	Positive
065	2023-05-26	Greenhill Observatory		K. Hill	1270	Merlin 247	GPS	Overcast
066	2023-05-26	Kuriwa Observatory		D. Gault	300	Watec WT-910BD	GPS	Negative
067	2023-05-26	Linden Observatory		T. Barry	750	Point Grey 28S5M	GPS	Negative
068	2023-05-26	Heaven's Mirror Observatory		W. Hanna	508	QHY174M	GPS	Negative
069	2023-05-26	Murrumbateman		D. Herald	400	Watec 910BD	GPS	Negative
070	2023-05-26	Flynn		J. Newman	35	Wat-910BD	GPS	Technical failure
071	2023-05-26		New Zealand	G. McKay	250	QHY174M	GPS	Positive
072	2023-05-26		New Zealand	R. Paine	235	QHY174M	GPS	Positive
073	2023-05-26		New Zealand	R. Glassey	405	ASI 178MM	NTP	Positive
074	2023-07-15	Albox		J. L. Maestre	406	Atik314L+		Subsampled Star
075	2023-07-15	TUBITAK (T100)		Y. Kilic	1000	SI 1100		Overcast
076	2023-07-15	Spain - OAJ		R. Iglesias-Marzoa	400	ProLine		Subsampled Star
077	2023-07-15	TTTT		M. R. Alarcon	800	QHY411M	GPS	Subsampled Star
078	2023-07-15	TTTT		M. R. Alarcon	800	QHY411M		Subsampled Star

Table 5 continued

Table 5 (continued)

id	Date	Site	Country	Observer	Ap. (mm)	Camera	Time	Status
079	2023-07-15	TÜBİTAK (T60)	Türkiye	Y. kilic	600	Andor iKon-L	GPS	Positive
080	2023-07-15	SLN	Italy	A. Frasca	910	Moravian-C4	GPS	Positive
081	2023-07-15	Artemis	Spain	A. Burdanov	1000	Andor iKon-L	GPS	Positive
082	2023-07-15	Calar Alto	Spain	J. L. Ortiz	1230	ASI-6200MM	GPS	Positive
083	2023-07-15	Liverpool	Spain	N. Morales	2000	RISE	GPS	Positive
084	2023-07-15	La Hita		N. Morales	770	SBIG-16803		Subsampled Star
085	2023-07-15	Sierra Nevada		J. L. Ortiz	1500	Andor iKon	GPS	No Data
086	2023-07-15	La Sagra		N. Morales	356	QHY174M	GPS	No Data
087	2023-07-15	Presa de Rules		A. Román	635	ASI 174 MM Mono		Negative
088	2023-07-15	MOSS		C. Rinner	500	ZWO6200		No Data
089	2023-07-15	A.S. Vidojevica	Serbia	D. Ilic	1400	Andor iKon-L	GPS	Positive
090	2023-07-15	TRAPPIST-North	Morocco	K. Barakoui	600	Andor iKONL	GPS	Positive
091	2023-07-15	BOOTES-2		E. J. Fernandez	600	Andor Ixon	GPS	Subsampled Star
092	2023-08-01	Tübingen University		R. Sfair	800	SBIG STL-1001E		Technical failure
093	2023-08-01	La Palma-Liverpool		N. Morales	2000	RISE		Subsampled Star
094	2023-08-01	Joan Oró Telescope	Spain	T. Santana-Ros	800	CCD42-40	NTP	Positive
095	2023-08-01	La Hita	Spain	N. Morales	770	SBIG-16803	GPS	Positive
096	2023-08-01	Calar Alto	Spain	N. Morales	600	ASI-6200MM	GPS	Positive
097	2023-08-01	Calar Alto	Spain	N. Morales	2200	Cafos		Positive
098	2023-08-24	GOA		M. Malacarne	304	ZWOASI1600MMPPro		Subsampled Star
099	2023-08-24	OACEP		F. Braga-Ribas	114	IMX224	GPS	Subsampled Star
100	2023-08-24	SONEAR3		C. Jacques	450	QHY600		Subsampled Star
101	2023-08-24	Spaceobs - ASH2		N. Morales	407	SBIG STL11000		Subsampled Star
102	2023-08-24	UEFG		M. Emilio	406	SBIG		Negative
103	2023-08-24	SOAR	Chile	J. I. B. Camargo	4100	Raptor 247	GPS	Technical failure
104	2023-08-24	OACEP	Brasil	F. Braga-Ribas	254	Raptor 247	GPS	Positive
105	2023-08-24	TRAPPIST-South	Chile	E. Jehin	600	FLI ProLine	GPS	Positive
106	2023-08-24	Danish	Chile	C. Snodgrass	1540	Andor - Ixon	GPS	Positive
107	2023-08-24	OPD	Brazil	C. L. Pereira	1600	iXon 4335	GPS	Positive
108	2024-04-10	OPD	Brasil	M. Emilio	1600	SPARC4	GPS	Positive
109	2024-04-10	OACEP	Brasil	F. B. Ribas	114	IMX224	NTP	Positive
110	2024-04-10	OASI	Brasil	E. Rondon	1000	Apo-U47	NTP	Positive
111	2024-04-10	IAG USP		M. F. Neto	406.4	Apogee Alta U9000		Overcast
112	2024-04-10		Brasil	C. L. Pereira	305	Raptor 247	GPS	Positive
113	2024-04-10	SONEAR3		C. Jacques	450.0	QHY600	NTP	Overcast
114	2024-04-10	UEFG	Brasil	M. L. Castranheira	304.8	ASI294MC	GPS	Positive
115	2024-04-10	UNESP - FEG		R. Sfair	406.0	Raptor 247	GPS	Overcast
116	2024-05-29		Australia	W. Hanna	508	QHY174M	GPS	Positive
117	2024-07-04	CAP	Spain	A. Selva	406	ZWO ASI	NTP	Positive
118	2024-07-04	OAJ	Spain	R. Iglesias-Marzoa	400	ProLine PL4720	NTP	Positive

Table 5 continued

Table 5 (continued)

id	Date	Site	Country	Observer	Ap. (mm)	Camera	Time	Status
119	2024-07-04		Schweiz	A. Schweizer	850	DVTH+CAM 432	GPS	Positive
120	2024-07-04	Borowiec	Poland	A. Marciniak	400	Andor Zyla	GPS	Positive
121	2024-07-04	La Hita	Spain	N. Morales	770	QHY174M	GPS	Positive
122	2024-07-04	Joan Oró Telescope	Spain	T. Santana-Ros	800	CCD42-40	NTP	Positive
123	2024-07-04		Belgium	O. Schreurs	406	Watec 910HX	GPS	Positive
124	2024-07-04	Chalin		M. K. Kaminska	700.0	FLI Kepler 4040		Subsampled Star
125	2024-07-04	Sierra Nevada		J. L. Ortiz	900.0	ANDOR	GPS	Negative
126	2024-07-04	La Hita		N. Morales	770.0	QHY174M	GPS	Subsampled Star
127	2024-07-04	BOTORRITA		O. Canales	500.0	QHY174	GPS	Technical failure
128	2025-06-12	Gemini North		C. L. Pereira	81000.0	'Alopeke	GPS	Negative
129	2025-06-12	CFHT		D. Souami	3580.0	WIRCam	GPS	Negative
130	2025-06-12	MIRA		K. Bender	203.0	Watec WAT-910HX	GPS	Subsampled Star
131	2025-06-12	BOOTES-2	Mexico - SPM	E. J. Fernandez	600	Ixon	GPS	Positive
132	2025-06-12		U.S.A	V. Nikitin	279	QHY174	GPS	Positive
133	2025-06-12		U.S.A	J. Dunham	356	QHY174M	GPS	Positive
134	2025-06-20	Calar Alto		J. L. Ortiz	1200.0	QHY600	GPS	Subsampled Star
135	2025-06-20	TUG		S. Eryilmaz	1000.0	SI 1100	GPS	Subsampled Star
136	2025-06-20	Joan Oró	Spain	T. Santana-Ros	800	CCD42-40	NTP	Positive
137	2025-06-20	ISTEK		M. Acar	300.0	QHY 5 III 178 M		Overcast
138	2025-06-20	IST40		S. Fişek	400.0	Moravian G2 8300	GPS	Overcast
139	2025-06-20	Ondokuz Mayıs		S. Kalkan	370.0	SBIG		Overcast
140	2025-06-20		Czechia	K. Hornoch	650	G2CCD-3200		Positive
141	2025-06-20	Piszkesteto	Hungary	A. Pal	1000	Andor iXon-888	GPS	Positive
142	2025-06-20	Sierra Nevada	Spain	F. J. Aceituno	1500	ANDOR	GPS	Positive
143	2025-06-20	Teplice		Z. Moravec	600.0	FLI Kepler FL4040		Subsampled Star
144	2025-06-20	OAJ	Spain	R. Iglesias-Marzoa	400	ProLine PL4720	NTP	Positive
145	2025-06-20	Bélesta	France	P. André	820	C3-PRO-61000	NTP	Positive
146	2025-06-20	TURKSAT		M. N. Bagiran	500.0	Kepler KL4040		Subsampled Star
147	2025-07-04	Sharjah	Emirates	Mohammad F. Talafha	431	SBIG	NTP	Positive
148	2025-07-04	Al Khatim		M. Odeh	356.0	ZWO ASI2600MM		Overcast
149	2025-07-04	Wise	U.S.A	S. Kaspi	457.2	QSI683		Negative
150	2025-07-04	Wise		S. Kaspi	800.0	QHY461		Negative
151	2025-07-04	Wise		S. Kaspi	711.0	FLI-PL16801		Negative
152	2025-07-04	KAO-Egypt		A. Takey	1880.0	E2V 42-40 2k	NTP	Overcast
153	2025-08-28	Westport		S. Diamond	356.0	QHY174M	GPS	Negative
154	2025-08-28	JJM Observatory		K. D. Green	430.0	QHY174M	GPS	Negative
155	2025-08-28	Mobile		V. Nikitin	279	QHY174M	GPS	Overcast
156	2025-08-28		U.S.A	S. Conard	356	Watec 910	GPS	Positive
157	2025-08-28		U.S.A	S. Conard	356	Watec 910	GPS	Positive
158	2025-08-28	Apache	U.S.A	M. Skrutskie	356	ASI432	GPS	Positive

Table 5 (continued)

Table 5 (*continued*)

id	Date	Site	Country	Observer	Ap. (mm)	Camera	Time	Status
159	2025-08-28	Apache	U.S.A	M. Skrutskie	356	ASI432	GPS	Positive
160	2025-08-31	LCO		J. M. Gómez-Limón Gallardo	350.0	QHY600		Technical failure
161	2025-08-31		Australia	D. Herald	508	Watec 910BD	GPS	Positive
162	2025-08-31		Australia	W. Hanna	508	QHY174M	GPS	Positive

Table 6. Observational data for all Quaoar events: Part 2 (Timing and Coordinates).

id	Exp (s)	Cycle (s)	Offset (s)	Latitude	Longitude	Height (m)	Ingress E. (s)	Egress E. (s)	Chord (km)	Chord e. (km)
001	2.135	2.135		39 08 58.73	-76 53 13.42	120.0	10:02:55.9	10:03:48.7	1059.1	53.5
002	2.0	2.0		-34 51 51.16	148 58 35.19	536.0	15:04:51.5	15:05:48.1	1143.7	18.7
003	2.56	2.56	-1.3	-34 57 31.6	148 59 54.80	594.0	15:04:50.8	15:05:47.2	1139.4	17.5
004	2.56	2.56	-1.3	-33 39 51.90	150 38 27.90	286.0	15:04:43.6	15:05:40.1	1141.2	16.8
005	1.0	1.0		-33 42 27.30	150 29 43.50	574.0	15:04:44.4	15:05:40.4	1130.9	9.0
006				-28 03 35.15	21 01 31.63	873.0	18:14:26.2	18:17:13.6	1107.5	0.7
007	6.0	6.0		-22 32 07.75	-45 34 57.54	1810.0	06:46:27.0	06:49:10.6	855.2	7.8
008	3.2	3.2	-4.8	-30 14 16.89	-70 44 21.12	2693.0	06:48:53.3	06:50:20.0	1092.7	39.2
009	15.0	15.98		-29 15 16.56	-70 44 21.84	2315.0	06:48:58.9	06:50:22.5	1054.1	24.9
010	30.0	31.0		44 07 58.213	26 13 07.378	90.0				
011	1.28	1.28		43 52 26.6	01 43 07.5	190.0				
012	10.0	12.0		50 55 19.5	-01 22 30.1	10.0				
013	5.0	5.0		37 59 52	23 53 35	165.0				
014	0.3	0.3		43 45 13.2000	06 55 22.700	1270.0				
015	2.0	2.4		37 45 06.000	38 13 32.000	700.0				
016	6.0	6.5		37 58 19.000	22 37 07.000	890.0				
017	1.6	1.6	-2.4	43 58 48.000	06 01 15.000	730.0				
018	7.0	7.11		46 13 54.000	27 40 10.000	70.0				
019	10.0	12.5		37 58 06.800	23 47 00.100	250.0				
020	1.0	1.0		45 47 22.00	07 28 42.00	1670.0	23:42:17.8	23:42:32.1	316.7	18.6
021	1.0	4.65		20 14 01.0	49 11 22.0	1786.0	23:41:16.9	23:42:03.7	1038.1	87.3
022	1.28	1.28	-0.66	52 15 09.66	08 19 24.16	220.0	23:41:50.2	23:42:38.5	1071.0	33.3
023	5.0	5.0		48 17 30.72	02 26 16.84	90.0	23:42:19.6	23:42:51.1	697.8	27.5
024	0.1302282	0.1348		28 45 21.60	-17 53 30.20	2270.0	03:00:08.45	03:00:55.32	1107.1	0.9
025										
026	5.0	6.0		31 12 22.32	-07 51 59.04	2777.0	02:59:32.5	03:00:12.2	900.8	19.3
027	8.0	11.65		28 17 57.30	-16 30 36.70	2390.0	03:00:00.1	03:00:53.9	1271.1	101.6
028	0.6	0.63		28 45 45.05	-17 52 45.12	2387.0	03:00:08.9	03:00:55.2	1094.1	9.1
029	2.5	3.78		28 18 02.00	-16 30 41.00	2440.0	03:00:01.5	03:00:49.6	1135.7	21.4
030	2.0	2.4961		-23 27 39.63	18 00 56.54	1340.0	17:27:54.4	17:28:56.2	1120.7	14.7
031										
032										
033	1.3	1.2139		-25 43 55.00	28 13 47.00	1300.0	19:04:39.9	19:07:09.1	1051.7	1.9
034	1.0	1.0	-1.5	-23 14 11.0	16 21 42.0	1834.0	19:02:28.6	19:05:03.2	1082.7	2.8
035	1.0	1.0	-1.5	-22 41 54.50	17 06 31.70	1910.0	19:02:28.9	19:05:03.5	1082.3	2.9
036	0.3	0.3	-0.45	-19 05 15.50	18 36 01.70	1200.0	19:02:36.86	19:04:38.05	848.0	0.6
037	1.5	2.44		-24 36 58.00	-70 23 26.00	2440.0	01:44:48.8	01:44:52.0	50.3	4.7
038	2.0	3.02		-30 10 03.52	-70 48 18.91	2200.0	01:44:10.5	01:45:18.4	1082.1	34.7

Table 6 continued

Table 6 (continued)

id	Exp (s)	Cycle (s)	Offset (s)	Latitude	Longitude	Height (m)	Ingress	E. (s)	Egress	E. (s)	Chord (km)	Chord e. (km)
039	3.0	4.12		-29 15 16.56	-70 44 21.84	2315.0	01:44:11.0	1.1	01:45:21.9	0.8	1130.5	29.3
040	1.068	1.068		33 49 00.10	-111 52 07.30	843.0	08:37:37.4	2.0	08:38:00.8	2.0	581.3	99.5
041	4.2291	4.235		33 48 42.90	-111 57 07.90	654.0	08:37:37.2	2.7	08:37:57.2	2.6	496.8	132.8
042	4.0	4.0		36 25 37.90	-87 41 43.80	90.0	08:36:13.3	0.7	08:36:38.3	5.8	617.5	160.9
043	0.5	0.5		34 53 34.32	-85 28 15.88	218.0	08:35:58.3	0.1	08:36:35.7	0.2	924.1	9.3
044	10.0	10.0		37 45 06.00	38 13 32.00	695.0	21:37:52.3	2.2	21:38:30.0	2.2	935.8	108.9
045	2.56	2.56	-1.3	-23 16 10.06	150 30 01.62	53.0	12:11:10.0	0.6	12:11:56.0	0.6	1150.1	31.7
046	0.133	0.133		36 18 20.8800	-121 33 59.7600	1603.0						
047				40 05 12.4008	-88 11 46.2984	224.0						
048				44 29 57.5232	-93 07 45.0480	289.46						
049				40 08 55.6008	-76 53 43.4796	181.6						
050				38 33 07.8012	-121 47 08.1600	18.0						
051				48 29 22.1364	-123 20 15.0433	34.36						
052	10.0	12.0		42 40 9.57	-71 07 19.056	71.64						
053	0.25	0.25	-0.15	36 18 20.8800	-121 33 59.7600	1603.0						
054	10.0	11.69		41 33 18.62	-72 39 33.12	68.0	08:40:01.0	6.6	08:41:01.9	2.5	985.6	148.6
055	15.0	20.59		43 47 30.59	-120 56 28.99	1907.0	08:43:54.0	5.2	08:44:35.5	5.9	653.3	178.8
056	2.0	2.0		49 32 01.67	-119 33 26.50	455.0	08:43:21.4	0.1	08:44:29.4	0.2	1093.1	5.8
057	1.3	1.3		49 00 32.18	-119 21 47.30	512.0	08:43:22.2	0.1	08:44:29.6	0.1	1083.8	3.2
058	2.0	2.94		28 18 02.00	-16 30 41.00	2440.0	00:28:32.2	0.6	00:28:44.1	0.9	218.0	27.5
059	0.64	0.64	-0.34	-43 59 12.0120	170 27 54.0000	1030.0						
060	0.64	0.64	-0.34	-34 57 31.3164	148 59 56.004	595.91						
061	0.266			-33 42 26.6868	150 29 43.4652	590.0						
062	0.5	0.5		-34 51 50.8900	148 58 35.0602	536.0						
063	0.64	0.64	-0.34	-23 16 10.06	150 30 01.62	53.0						
064	0.32	0.32	-0.18	-45 52 21.37	170 29 29.86	103.0	14:37:52.2	0.1	14:38:42.5	0.1	996.7	4.0
065				-42 25 51.8160	147 43 10.5600	646.0	15:51:38.6	0.1	15:52:33.5	0.1	1116.6	1.9
066	0.64	0.64	-0.34	-33 39 52.4844	150 38 27.9600	273.17						
067	0.266			-33 42 26.6868	150 29 43.4652	590.0						
068	0.25	0.25		-34 51 50.8900	148 58 35.0602	536.0						
069	0.32	0.32	-0.18	-34 57 31.3164	148 59 56.004	595.91						
070	0.64	0.64		-35 11 55.3400	149 02 57.5300	657.0						
071	4.0	4.0		-41 32 08.66	173 57 25.31	14.0			15:52:11.6	0.7		
072	2.0	2.0		-45 02 44.80	169 12 36.70	200.0	15:51:42.6	0.2	15:52:38.5	0.2	1137.3	9.7
073	2.0	2.53		-43 29 55.35	172 20 59.03	103.0	15:51:31.5	0.5	15:52:24.8	0.5	1083.7	20.8
074	15.0			37 24 20.0304	-2 09 06.4800	491.0						
075				36 49 17.4000	30 20 07.9846	2538.72						
076	13.0			40 02 30.4800	-1 00 58.6800	1957.0						
077	4.53			28 17 55.3633	-16 30 34.1358	2359.11						
078	4.53			28 17 55.3604	-16 30 34.4481	2359.12						

Table 6 continued

Table 6 (continued)

id	Exp (s)	Cycle (s)	Offset (s)	Latitude	Longitude	Height (m)	Ingress	E. (s)	Egress	E. (s)	Chord (km)	Chord e. (km)
079	8.0	13.2		36 49 29.00	30 20 08.28	2455.0	00:13:03.1	3.4	00:13:43.7	3.5	973.7	166.9
080	8.0	8.22		37 41 05.00	14 58 04.01	1735.0	00:13:42.3	2.2	00:14:26.7	0.4	1067.2	62.9
081	6.0	6.93		28 18 02.00	-16 30 41.00	2440.0	00:15:31.4	2.2	00:16:17.1	1.1	1102.8	80.1
082	4.0	5.61		37 13 24.71	-02 32 44.88	2173.0	00:14:50.1	1.4	00:15:10.0	0.7	480.0	48.3
083	3.0	3.03		28 45 45.05	-17 52 45.12	2387.0	00:15:37.0	1.0	00:16:21.8	1.1	1080.2	50.0
084	7.0			39 34 04.8000	-3 10 59.8800	770.0						
085				37 03 50.8896	-3 23 04.9200	2930.53						
086				37 58 51.6000	-2 33 50.4000	1530.0						
087	4.319			36 51 07.6603	-3 30 12.5857	155.21						
088				31 12 23.6052	-7 51 58.9248	2750.0						
089	4.0	5.0		43 08 24.6	21 33 21.4	1150.0	00:13:43.9	1.4	00:14:02.8	0.3	452.9	40.9
090	6.0	6.86		31 12 22.32	-07 51 59.04	2777.0	00:14:57.1	0.6	00:15:41.7	0.9	1077.8	37.6
091	10.0			36 45 33.2676	-4 02 27.4920	70.0						
092	1.0			48 32 03.0156	9 04 12.0036	400.0						
093	5.0			28 45 45.0576	-17 52 45.1200	2387.63						
094	20.0	23.2		42 03 05.96	00 43 46.74	1564.0	22:17:08.2	9.1	22:17:53.8	7.2	936.4	334.7
095	25.0	27.9		39 34 04.80	-03 10 59.88	770.0	22:17:26.8	11.3	22:18:05.4	11.9	793.2	476.8
096	30.0	30.8		37 13 24.71	-02 32 44.88	2173.0	22:17:18.3	5.6	22:18:08.8	7.4	1038.4	267.3
097	20.0	35.0		37 13 24.71	-02 32 44.88	2173.0	22:17:14.0	8.2	22:18:08.4	1.3	1118.6	195.3
098	15.0			-20 18 01.99998	-40 19 02.0000	24.0						
099	4.0			-25 20 57.3942	-49 21 55.4240	1055.01						
100	2.0			-19 49 27.2635	-43 41 24.0250	1498.97						
101	8.0			-22 57 10.8000	-68 10 44.4000	2400.0						
102				-25 05 22.1251	-50 05 56.3925	909.79						
103	1.0	1.0	-1.5	-30 14 16.89	-70 44 21.12	2693.0	03:18:39.4	0.1	03:19:33.3	0.1	711.7	3.1
104	5.0	5.0	-7.5	-25 20 57.39	-49 21 55.42	1055.0	03:16:21.2	0.5	03:17:45.7	0.5	1106.5	12.4
105	5.0	7.64		-29 15 16.56	-70 44 21.84	2315.0	03:18:47.3	1.6	03:19:18.1	2.3	406.1	50.6
106	0.1	0.101		-29 15 31.76	-70 44 01.46	2345.0	03:18:46.82	0.01	03:19:17.85	0.02	409.1	0.4
107	0.4	0.43		-22 32 07.75	-45 34 57.54	1810.0	03:15:53.5	0.1	03:17:16.6	0.3	1084.8	4.4
108	2.0	4.64		-22 32 07.75	-45 34 57.54	1810.0	03:53:58.8	1.4	03:57:20.6	1.5	815.9	11.4
109	2.5	2.5		-25 20 57.39	-49 21 55.42	1055.0	03:52:54.2	0.2	03:55:21.0	0.3	592.5	2.1
110	5.0	6.8		-08 47 32.10	-38 41 18.70	390.0	04:00:06.4	0.1	04:04:20.1	0.1	1030.1	0.5
111				-23 00 09	-46 57 55	870.0						
112	1.0	1.0	-1.5	-25 13 39.65	-50 36 41.71	968.0	03:53:07.1	0.1	03:55:06.3	0.1	480.5	0.8
113				-19 49 27.2635	-43 41 24.0250	1498.97						
114	3.0	3.35		-25 05 22.15	-50 05 56.40	909.0	03:53:09.3	0.2	03:55:15.8	0.1	510.3	1.2
115				-22 48 06.0012	-45 11 25.5984	540.0						
116	20.0	20.0		-34 51 50.89	148 58 35.06	536.0	19:12:28.9	4.6	19:13:13.3	4.0	928.3	179.8
117	3.0	3.1		42 13 42.95	1 44 16.37	1185.0	22:57:28.4	0.6	22:58:05.2	0.6	919.6	31.3
118	7.0	7.4		40 02 30.48	-01 00 58.68	1957.0	22:57:44.6	2.2	22:58:08.2	3.1	589.7	131.8

Table 6 continued

Table 6 (continued)

id	Exp (s)	Cycle (s)	Offset (s)	Latitude	Longitude	Height (m)	Ingress	E. (s)	Egress	E. (s)	Chord (km)	Chord e. (km)
119	0.9	0.9	1.35	47 31 10.48	8 34 14.32	546.0	22:56:59.3	0.3	22:57:44.2	0.1	1119.0	10.7
120	5.0	5.0		52 16 36.87	17 04 30.75	83.0	22:56:35.1	2.4	22:57:18.5	1.7	1082.4	101.6
121	3.0	3.0		39 34 04.80	-03 10 59.88	770.0	22:57:54.2	2.6				
122	10.0	13.7		42 03 05.96	00 43 46.74	1564.0	22:57:28.8	3.5	22:58:09.5	2.7	1016.5	155.5
123	2.56	2.56	-1.3	50 31 24.93	05 26 29.36	261.0	22:57:08.0	0.2	22:57:51.8	0.7	1092.6	23.4
124	1.0			52 36 14.0270	16 02 33.4403	65.0						
125	5.0			37 03 50.8896	-3 23 04.9200	2930.53						
126				39 34 04.8000	-3 10 59.8800	770.0						
127				41 29 50.5500	-1 01 15.1212	403.0						
128	0.1			19 49 25.7016	-155 28 08.6160	4213.0						
129	0.1			19 49 31.0080	-155 28 07.9320	4206.11						
130	0.266	0.266	-0.15	36 18 21.0069	-121 34 00.3195	1520.42						
131	5.0	5.0	-7.5	31 02 36.26	-115 27 47.88	2824.0	09:52:13.2	0.2	09:53:01.4	0.3	1036.6	9.0
132	2.5	2.5		37 12 37.99	-104 29 57.23	1862.0	09:51:44.4	1.2	09:52:16.2	1.4	744.8	62.5
133	4.0	4.0		33 37 29.20	-111 43 38.31	520.0	09:52:02.5	0.2	09:52:46.6	0.2	1036.6	9.0
134	8.0			37 13 24.7116	-02 32 44.8800	2173.21						
135	15.0			36 49 17.2200	30 20 07.9836	2538.72						
136	20.0	21.9		42 3 5.95	00 43 46.74	1564.0	23:47:00.9	4.8	23:47:48.3	5.2	1166.4	239.6
137				41 01 49.0476	29 02 33.3996	110.0						
138				41 00 42.2964	28 57 56.5848	60.0						
139				41 22 03.8172	36 12 05.6736	150.0						
140	5.0	6.2		49 54 38.016	14 47 01.10	528.0	23:46:18.1	1.2	23:46:54.5	1.5	896.8	71.8
141	2.0	2.0		47 55 04.96	19 53 39.48	932.0	23:46:00.5	0.9	23:46:41.9	0.6	1015.2	34.3
142	10.0	11.5		37 03 50.88	-03 23 4.92	2930.0	23:47:24.5	2.3	23:47:58.0	1.6	825.5	99.2
143	5.0			50 38 17.9556	13 50 48.3000	277.94						
144	15.0	15.4		40 02 30.48	-01 00 58.68	1957.0	23:47:07.0	7.7	23:47:56.1	5.1	1196.8	361.7
145	5.0	5.5		43 26 43	01 49 03	247.0	23:46:56.6	0.8	23:47:42.7	1.2	1133.5	49.5
146				39 38 11.8752	32 48 14.9652	950.0						
147	5.0	7.0		25 16 56.92	55 27 42.95	50.0	23:02:54.9	1.5	23:03:36.6	0.5	1044.4	48.4
148				24 13 10.5780	54 55 12.6912	90.0						
149	4.0			30 35 48.5862	34 45 44.1366	862.27						
150	4.0			30 35 48.5862	34 45 44.1366	862.27						
151	4.0			30 35 48.5862	34 45 44.1366	862.27						
152	153	0.125		29 56 02.4000	31 49 37.2000	476.0						
153				41 10 15.8999	-73 19 39.2999	88.0						
154	2.0			41 31 32.6064	-73 25 33.8160	76.87						
155	2.0	2.0		39 25 51.12	-103 15 59.27	1559.0						
156	0.533	0.533	-0.284	41 44 48.79	-77 19 0.39	436.0	02:38:41.0	1.2	02:38:58.5	1.5	220.7	31.7
157	0.533	0.533	-0.284	41 44 48.79	-77 19 0.39	436.0	02:39:07.9	0.5	02:40:00.4	0.5	656.6	12.1
158	0.1	0.1	13.6	32 46 49.80	-105 49 14.08	2791.0	02:41:29.7	0.5	02:42:49.3	0.5	1002.6	12.6

Table 6 continued

Table 6 (continued)

id	Exp (s)	Cycle (s)	Offset (s)	Latitude	Longitude	Height (m)	Ingress	E. (s)	Egress	E. (s)	Chord (km)	Chord e. (km)
159	0.1	0.1	13.6	32 46 49.80	-105 49 14.08	2791.0	02:42:00.3	20.0	02:43:33.8	0.2	1177.7	254.4
160	3.0			-31 16 22.5696	149 04 14.9160	1118.33						
161	2.56	2.56	-1.3	-34 57 31.31	148 59 56.00	595.0	13:41:16.6	0.5	13:42:59.1	0.9	1130.3	14.8
162	5.0	5.0		-34 51 50.89	148 58 35.06	536.0	13:41:15.1	0.7	13:42:55.7	0.7	1108.5	16.2

REFERENCES

- Arimatsu, K., Ohsawa, R., Hashimoto, G. L., et al. 2019, *AJ*, 158, 236, doi: [10.3847/1538-3881/ab5058](https://doi.org/10.3847/1538-3881/ab5058)
- Assafin, M. 2023a, *Planet. Space Sci.*, 238, 105801, doi: [10.1016/j.pss.2023.105801](https://doi.org/10.1016/j.pss.2023.105801)
- . 2023b, *Planet. Space Sci.*, 239, 105816, doi: [10.1016/j.pss.2023.105816](https://doi.org/10.1016/j.pss.2023.105816)
- Astropy Collaboration, Price-Whelan, A. M., Lim, P. L., et al. 2022, *ApJ*, 935, 167, doi: [10.3847/1538-4357/ac7c74](https://doi.org/10.3847/1538-4357/ac7c74)
- Barry, M. A. T., Gault, D., Bolt, G., et al. 2015, *PASA*, 32, e014, doi: [10.1017/pasa.2015.15](https://doi.org/10.1017/pasa.2015.15)
- Bernardes, D., Junior, O. V., Rodrigues, F., et al. 2025, *PASP*, 137, 035003, doi: [10.1088/1538-3873/ada187](https://doi.org/10.1088/1538-3873/ada187)
- Braga-Ribas, F., Vachier, F., Desmars, J., Margoti, G., & Sicardy, B. 2025, *Philosophical Transactions A*, 383, 20240200
- Braga-Ribas, F., Sicardy, B., Ortiz, J. L., et al. 2013, *ApJ*, 773, 26, doi: [10.1088/0004-637X/773/1/26](https://doi.org/10.1088/0004-637X/773/1/26)
- Brown, M. E., & Suer, T. A. 2007, *IAUC*, 8812, 1
- Desmars, J., Camargo, J. I. B., Braga-Ribas, F., et al. 2015, *A&A*, 584, A96, doi: [10.1051/0004-6361/201526498](https://doi.org/10.1051/0004-6361/201526498)
- Dhillon, V. S., Bezawada, N., Black, M., et al. 2021, *MNRAS*, 507, 350, doi: [10.1093/mnras/stab2130](https://doi.org/10.1093/mnras/stab2130)
- Dias-Oliveira, A., Sicardy, B., Lellouch, E., et al. 2015, *ApJ*, 811, 53, doi: [10.1088/0004-637X/811/1/53](https://doi.org/10.1088/0004-637X/811/1/53)
- Dias-Oliveira, A., Sicardy, B., Ortiz, J. L., et al. 2017, *AJ*, 154, 22, doi: [10.3847/1538-3881/aa74e9](https://doi.org/10.3847/1538-3881/aa74e9)
- Fortin, F.-A., De Rainville, F.-M., Gardner, M.-A. G., Parizeau, M., & Gagné, C. 2012, *The Journal of Machine Learning Research*, 13, 2171
- Fraser, W. C., Batygin, K., Brown, M. E., & Bouchez, A. 2013, *Icarus*, 222, 357, doi: [10.1016/j.icarus.2012.11.004](https://doi.org/10.1016/j.icarus.2012.11.004)
- French, R. G., & Gierasch, P. J. 1976, *AJ*, 81, 445, doi: [10.1086/111905](https://doi.org/10.1086/111905)
- Gaia Collaboration, Brown, A. G. A., Vallenari, A., et al. 2018, *A&A*, 616, A1, doi: [10.1051/0004-6361/201833051](https://doi.org/10.1051/0004-6361/201833051)
- . 2021, *A&A*, 649, A1, doi: [10.1051/0004-6361/202039657](https://doi.org/10.1051/0004-6361/202039657)
- Gazeas, K. 2016, in *Revista Mexicana de Astronomía y Astrofísica Conference Series*, Vol. 48, *Revista Mexicana de Astronomía y Astrofísica Conference Series*, 22–23
- Gomes-Júnior, A. R., Morgado, B. E., Benedetti-Rossi, G., et al. 2022, *MNRAS*, 511, 1167, doi: [10.1093/mnras/stac032](https://doi.org/10.1093/mnras/stac032)
- Hanisch, R. J., Farris, A., Greisen, E. W., et al. 2001, *Astronomy & Astrophysics*, 376, 359
- Harris, C. R., Millman, K. J., Van Der Walt, S. J., et al. 2020, *Nature*, 585, 357
- Jehin, E., Gillon, M., Queloz, D., et al. 2011, *The Messenger*, 145, 2
- Johnson, T. V., & McGetchin, T. R. 1973, *Icarus*, 18, 612, doi: [10.1016/0019-1035\(73\)90064-X](https://doi.org/10.1016/0019-1035(73)90064-X)
- Kilic, Y., Braga-Ribas, F., Kaplan, M., et al. 2022, *MNRAS*, 515, 1346, doi: [10.1093/mnras/stac1595](https://doi.org/10.1093/mnras/stac1595)
- Kiss, C., Müller, T. G., Marton, G., et al. 2024, *A&A*, 684, A50, doi: [10.1051/0004-6361/202348054](https://doi.org/10.1051/0004-6361/202348054)
- Klioner, S. A. 2003, *AJ*, 125, 1580, doi: [10.1086/367593](https://doi.org/10.1086/367593)
- Leiva, R., Sicardy, B., Camargo, J. I. B., et al. 2017, *AJ*, 154, 159, doi: [10.3847/1538-3881/aa8956](https://doi.org/10.3847/1538-3881/aa8956)
- Lykawka, P. S., & Mukai, T. 2007, *Icarus*, 189, 213, doi: [10.1016/j.icarus.2007.01.001](https://doi.org/10.1016/j.icarus.2007.01.001)
- Margoti, G. 2024, Master's thesis, Universidade Tecnológica Federal do Paraná
- Morgado, B. E., Sicardy, B., Braga-Ribas, F., et al. 2021, *A&A*, 652, A141, doi: [10.1051/0004-6361/202141543](https://doi.org/10.1051/0004-6361/202141543)
- Morgado, B. E., Bruno, G., Gomes-Júnior, A. R., et al. 2022, *A&A*, 664, L15, doi: [10.1051/0004-6361/202244221](https://doi.org/10.1051/0004-6361/202244221)
- Morgado, B. E., Sicardy, B., Braga-Ribas, F., et al. 2023, *Nature*, 614, 239, doi: [10.1038/s41586-022-05629-6](https://doi.org/10.1038/s41586-022-05629-6)
- Nolthenius, R., Bender, K., Cotton, D. V., Proudfoot, B. C. N., & Irwin, J. 2025, *Research Notes of the American Astronomical Society*, 9, 226, doi: [10.3847/2515-5172/adfed4](https://doi.org/10.3847/2515-5172/adfed4)
- Ortiz, J. L., Gutiérrez, P. J., Sota, A., Casanova, V., & Teixeira, V. R. 2003, *A&A*, 409, L13, doi: [10.1051/0004-6361:20031253](https://doi.org/10.1051/0004-6361:20031253)
- Ortiz, J. L., Sicardy, B., Braga-Ribas, F., et al. 2012, *Nature*, 491, 566, doi: [10.1038/nature11597](https://doi.org/10.1038/nature11597)
- Pavlov, H., Anderson, R., Barry, T., et al. 2020, *Journal for Occultation Astronomy*, 10, 8
- Pedregosa, F., Varoquaux, G., Gramfort, A., et al. 2011, *Journal of Machine Learning Research*, 12, 2825, doi: [10.48550/arXiv.1201.0490](https://doi.org/10.48550/arXiv.1201.0490)
- Pereira, C. L., Sicardy, B., Morgado, B. E., et al. 2023, *A&A*, 673, L4, doi: [10.1051/0004-6361/202346365](https://doi.org/10.1051/0004-6361/202346365)
- Person, M. J., Elliot, J. L., Bosh, A. S., et al. 2011, in *American Astronomical Society Meeting Abstracts*, Vol. 218, *American Astronomical Society Meeting Abstracts #218*, 224.12
- Poiani, M., Gomes-Júnior, A. R., Camargo, J. I. B., et al. 2026
- Proudfoot, B., Holler, B. J., Arimatsu, K., et al. 2025, *PSJ*, 6, 146, doi: [10.3847/PSJ/addd02](https://doi.org/10.3847/PSJ/addd02)
- Rabinowitz, D. L., Schaefer, B. E., & Tourtellotte, S. W. 2007, *AJ*, 133, 26, doi: [10.1086/508931](https://doi.org/10.1086/508931)
- Rizos, J. L., Ortiz, J. L., Rommel, F. L., et al. 2025, *A&A*, 697, A62, doi: [10.1051/0004-6361/202554154](https://doi.org/10.1051/0004-6361/202554154)
- Rodríguez, A., Morgado, B. E., & Callegari, Jr., N. 2023, *MNRAS*, 525, 3376, doi: [10.1093/mnras/stad2413](https://doi.org/10.1093/mnras/stad2413)

- Rommel, F. L., Braga-Ribas, F., Desmars, J., et al. 2020, *A&A*, 644, A40, doi: [10.1051/0004-6361/202039054](https://doi.org/10.1051/0004-6361/202039054)
- Rommel, F. L., Fernández-Valenzuela, E., Proudfoot, B. C. N., et al. 2025, *PSJ*, 6, 48, doi: [10.3847/PSJ/adabc1](https://doi.org/10.3847/PSJ/adabc1)
- Rossi, A., Marzari, F., & Farinella, P. 1999, *Earth, Planets and Space*, 51, 1173, doi: [10.1186/BF03351592](https://doi.org/10.1186/BF03351592)
- Sicardy, B. 2023, *Comptes Rendus Physique*, 23, 213, doi: [10.5802/crphys.109](https://doi.org/10.5802/crphys.109)
- Sicardy, B., Braga-Ribas, F., Buie, M. W., Ortiz, J. L., & Roques, F. 2024, *A&A Rv*, 32, 6, doi: [10.1007/s00159-024-00156-x](https://doi.org/10.1007/s00159-024-00156-x)
- Sicardy, B., & Dettwiller, L. 2025, *A&A*, submitted
- Tancredi, G., & Favre, S. 2008, *Icarus*, 195, 851, doi: [10.1016/j.icarus.2007.12.020](https://doi.org/10.1016/j.icarus.2007.12.020)
- Vachier, F., Berthier, J., & Marchis, F. 2012, *A&A*, 543, A68, doi: [10.1051/0004-6361/201118408](https://doi.org/10.1051/0004-6361/201118408)
- Van Belle, G. T. 1999, *Publications of the Astronomical Society of the Pacific*, 111, 1515
- Young, L. A., Braga-Ribas, F., & Johnson, R. E. 2020, in *The Trans-Neptunian Solar System*, ed. D. Prialnik, M. A. Barucci, & L. Young, 127–151, doi: [10.1016/B978-0-12-816490-7.00006-0](https://doi.org/10.1016/B978-0-12-816490-7.00006-0)